



NASA TN D-2769

FACILITY FORM 802

N65 23162
 (ACCESSION NUMBER) _____ (THRU) _____
LB
 (PAGES) _____ (CODE) _____
 _____ (CATEGORY) _____
 (NASA CR OR TMX OR AD NUMBER)

GPO PRICE \$ _____
 CPST
 GTS PRICE(S) \$ 2.00

Hard copy (HC) _____

Microfiche (MF) .50

**TECHNIQUE FOR MEASURING
 HIGH-TEMPERATURE ISOTHERM PATTERNS
 ON AERODYNAMICALLY HEATED MODELS
 WITH EXPERIMENTAL RESULTS**

by Irving Weinstein and Robert R. Howell

*Langley Research Center
 Langley Station, Hampton, Va.*

TECHNIQUE FOR MEASURING HIGH-TEMPERATURE ISOTHERM
PATTERNS ON AERODYNAMICALLY HEATED MODELS
WITH EXPERIMENTAL RESULTS

By Irving Weinstein and Robert R. Howell

Langley Research Center
Langley Station, Hampton, Va.

NATIONAL AERONAUTICS AND SPACE ADMINISTRATION

For sale by the Clearinghouse for Federal Scientific and Technical Information
Springfield, Virginia 22151 - Price \$2.00

TECHNIQUE FOR MEASURING HIGH-TEMPERATURE ISOTHERM

PATTERNS ON AERODYNAMICALLY HEATED MODELS

WITH EXPERIMENTAL RESULTS

By Irving Weinstein and Robert R. Howell
Langley Research Center

SUMMARY

23/62

An investigation was made to determine the accuracy and detail to which temperatures and the variations in temperature over the surface of aerodynamically heated ceramic models of hypersonic vehicles can be measured with a photographic pyrometer. The models were cast from a ceramic material which could withstand the test temperatures without melting and reach surface equilibrium temperatures within the available test period. Tests were conducted on several configurations of these ceramic models in a test medium of methane-air combustion products at a nominal Mach number of 7.0, at total temperatures from approximately 2700° F (1756° K) to 3180° F (2022° K), and at model stagnation-point pressures from 5 to 17 psia (34 to 117 kN/m²). The corresponding range of free-stream Reynolds numbers varied from 0.44×10^6 to 1.58×10^6 per foot (1.44 to 5.19 per μm).

The results of this investigation indicate that the technique can be used to determine the surface temperatures and nondimensional heating-rate ratios with reasonable accuracy. This technique also provides ready definition of the areas of increased heating on the surface resulting from surface irregularities or component interference. Isotherm patterns are presented over the surfaces of several configurations which show the detail to which the variations in surface heating can be detected.

INTRODUCTION

In the analysis of the structural thermal-protection requirements of most hypersonic vehicles it is necessary to have a knowledge of the heating-rate distribution and the resulting equilibrium temperature distribution over the vehicle surface. For simple bodies of revolution the assumption of Newtonian flow permits the application of theory which yields satisfactory results for cases in which flow separation or boundary-layer transition is not a factor. When the vehicle geometry is such that flow separation is significant over large areas of the surface, or over areas which are subject to flow detachment, shock impingement, or component interference, accurate distributions of heating rate

and equilibrium temperature can be better achieved by testing a model of the vehicle under simulated flight conditions.

In order to measure the desired temperature and heating-rate distributions on wind-tunnel models by conventional test methods, such as with thermocouple or calorimeter installations, the sensing elements must be installed in a closely knit array of measurement locations, usually on small models. The combination of a large number of measuring points and small models make such tests costly and difficult and, in some cases, impossible. Hence, other methods of obtaining the desired measurements are needed.

One method that has been used with some success is to paint a test model with temperature-sensitive paint and subject it to aerodynamic heating in a hypersonic stream. (See, for example, refs. 1 and 2.) By proper analysis of the resulting paint-color distribution, nondimensional heating-rate distributions can be deduced. Although the overall heating patterns afforded by this technique are generally correct, they are dependent upon the interpretation of the shades of the color changes of the paint and they are usually restricted to temperatures below about 1200° F (922° K).

The present paper describes a technique for obtaining the temperature and heating-rate distributions on models immersed in a hypersonic flow which has a realistic energy level. The technique involves molding a model of a low-conductivity slip-cast fused silica, heating the model aerodynamically in a hypersonic environment, and measuring the isotherm patterns on the model with a photographic pyrometer, or photometer, as described in reference 3. This technique provides a means of predicting the values of surface temperature which a hypersonic vehicle experiences in flight, as well as the nondimensional heating-rate ratios over the surface.

Experimental results obtained from a number of hypersonic models tested in the 7-inch Mach 7 pilot tunnel at the Langley Research Center are also presented and discussed.

SYMBOLS

The units used for the physical quantities defined in this paper are given both in the U.S. Customary Units and in the International System of Units (SI). Factors relating the two systems are given in reference 4.

h film heat-transfer coefficient, $\frac{\text{Btu}}{\text{ft}^2\text{-sec-}^\circ\text{F}}$ ($\text{W/m}^2\text{-}^\circ\text{K}$)

\dot{q} convective heat-transfer rate, $\frac{\text{Btu}}{\text{ft}^2\text{-sec}}$ (W/m^2)

r radius, inches (centimeters)

R	free-stream Reynolds number
s	distance along model surface from center of face, inches (centimeters)
t	time, seconds
T	temperature, °F or °R (°K)
x	length measured along model center line from extended apex of model, inches (centimeters)
α	angle of attack, degrees
ε	emissivity
θ	angle between model center line and ray through extended apex of model, degrees
λ	wave length, microns
σ	Stefan-Boltzmann constant, $0.477 \times 10^{-12} \frac{\text{Btu}}{\text{ft}^2\text{-sec-}^\circ\text{F}^4} \quad \left(5.6697 \times 10^{-8} \text{ W/m}^2\text{-}^\circ\text{K}^4\right)$

Subscripts:

aw	adiabatic wall
¢	center line
eq	equilibrium
i	indicated
l	local condition
le	leading edge
o	reference
s	stagnation
t	total
w	wall

GENERAL DESCRIPTION OF TECHNIQUE

The present technique for defining temperature distributions or isotherm patterns on vehicle surfaces involves subjecting a correctly detailed model to a hypersonic stream which simulates a realistic environment for the flight vehicle. To facilitate measurement of surface temperatures, the model should be constructed of a material having low heat capacity and thermal conductivity, so that the model surface rapidly approaches an equilibrium temperature distribution when immersed in the stream. This distribution of equilibrium temperatures on the model represents the maximum temperatures an aircraft would reach during extremely long flights in an environment corresponding to the model test conditions. The temperature distribution can then be read out with the use of a photographic pyrometer which records on film the level of intensity of the heated surface. A densitometer was then used to read out the film density at various locations on a projected image of the model surface. The surface temperature was related to the image density through a calibration procedure in which a tungsten lamp filament of known temperature and emissivity was photographed.

Local convective heating rates can be calculated from equilibrium temperatures from the following relation under the condition that the conduction is small:

$$\dot{q} = h(T_{aw} - T_{eq}) = \sigma\epsilon(T_{eq}^4 - T_w^4) \quad (1)$$

Under most conditions for which photometric pyrometry is applicable, T_w is small compared with T_{eq} ; therefore,

$$\dot{q} = \sigma\epsilon T_{eq}^4 \quad (2)$$

where only the emissivity of the surface and the equilibrium temperature are required for the computations. A nondimensional heating-rate ratio can then be

written as $\frac{\dot{q}}{\dot{q}_s} = \frac{\epsilon}{\epsilon_s} \left(\frac{T_{eq}}{T_{eq,s}} \right)^4$. If the total emissivity is the same at both points, this equation reduces to

$$\frac{\dot{q}}{\dot{q}_s} = \left(\frac{T_{eq}}{T_{eq,s}} \right)^4 \quad (3)$$

The use of the photographic pyrometer to determine the surface temperatures requires that the model surface be heated to incandescence. The present technique, therefore, is limited to test facilities whose stream energy level is of

the order of 1000 Btu/lb (2.32 kJ/g) or greater (to obtain surface incandescence) and whose running times are sufficiently long for the surface temperatures to approach equilibrium. It is also limited to regions on the test model where heating rates are sufficiently large to bring the surface temperatures into the visible range. In most cases the regions of high heating rate on hypersonic vehicles are the areas of major concern.

MODEL FABRICATION

Material

The model material requirements for satisfactory performance of the technique are as follows: (1) The material must have low thermal conductivity and heat capacity in order that the surface temperature approach equilibrium values rapidly and that conduction effects on the temperature distributions be small. (2) The material must have a high melting point and a high resistance to thermal shock in order to withstand the large temperature gradients near the stagnation region, as well as rapid heating without melting or cracking. (3) The material must have satisfactory fabrication characteristics; that is, models of fine detail must be producible from the material. (4) The cost and man-hours for model fabrication must be reasonable.

A material which demonstrates these requirements and which was used for the present model construction is slip-cast fused silica. Basic properties of the material are presented in table I. This material is a ceramic which is bought in slip form and is composed of 99.8 percent fused silica with aluminum oxide (Al_2O_3) being the major impurity. It is easily cast to the desired shape. In the cured state the material is white and porous and the outer surface is very smooth and hard. A major disadvantage of the material is its relatively low tensile strength which necessitates avoiding thin sections which are heavily loaded in bending.

Fabrication Technique

As previously stated, the present models were slip cast from the fused silica. The molds in which the castings are made were formed with a pattern of the exact size of the desired model. (Shrinkage of the castings is negligible.) Molds were made from a pottery plaster mixture which afforded the desired porosity and dryness necessary to the slip-casting process. After the slip is poured into the mold, the liquid which suspends the silica is absorbed by the mold and the silica is deposited on the mold surface. After several minutes the excess slip is poured out, leaving a shell of the model of the desired thickness in the mold. This shell is extracted from the mold and subjected to an oven-curing process at temperatures up to 2100° F (1422° K). Upon completion of the cure, a tunnel support adapter is potted into the cavity of the shell, and a coarser grade of the silica slip is used. The potting material is then cured, completing the fabrication process. The total process for an average configuration from the pattern construction through the completed model requires about 300 man-hours of work with about half of this time usually

being required for the pattern construction. The mold can be reused to turn out a number of models of the same configuration if desired.

Typical models which have been fabricated in the preceding manner and used to obtain such data as presented in later sections of the paper are shown in the photographs and sketches of figures 1 to 4. The models were all sanded prior to testing in an attempt to smooth the surfaces and remove the excess material buildup along the mold parting lines.

SURFACE TEMPERATURE RECORDING SYSTEM

Photographic Pyrometer

In order to obtain the surface temperature distributions on the ceramic models, a photographic pyrometer was used to record the temperatures photographically. An investigation and calibration of this technique has previously been made and reported in reference 3. This system records temperatures by exposing a photographic emulsion to the visible radiation from the incandescent surface of the models. The density of the resulting negative image can then be related to the surface temperature of the model by means of a calibration. Data readout was made with the use of a densitometer which determined the relative density at the desired points on the image of the model surface. Calibrations were made with a source of known temperature and emissivity to relate the negative density to temperature. From the calibration the temperature can be determined at any desired point on the surface which has been heated to incandescence.

For the present system, a K-24 aerial camera modified to take pictures simultaneously through four matched lenses was used as the photometer. (See fig. 3 of ref. 3.) Neutral density filters of a predetermined value were placed in front of the four lenses to vary the amount of light intensity being transmitted through each lens. The four filters permitted temperature readings to be made over a range from the minimum value of about 1550° F (1117° K) to approximately 2250° F (1506° K). Another group of more dense filters was used for temperatures from about 1950° F (1339° K) to 2750° F (1783° K).

Calibration

The calibration procedure for the photographic pyrometer followed that described in reference 3. Pictures were taken of the incandescent surface of a tungsten filament lamp with black and white film in the modified K-24 aerial camera. The temperature of the filament was determined with an optical pyrometer; this instrument indicates the brightness temperature, which is a function of the filament emissivity. A correction for emissivity gives the true temperature of the filament. Exposures were taken of the lamp through each lens at a series of known temperatures. A curve could then be plotted at each temperature of the resulting film densities against the relative exposure of the neutral density filters. A ratio of intensities can then be obtained between each of these temperatures and the desired calibrate temperature. This ratio can be

used to obtain a master curve which relates the variation of exposure to the temperature. The calibrations were made for these tests by using a true temperature of about 2000° F (1367° K) for use with the lower temperature range previously mentioned and a temperature of about 2400° F (1589° K) for the higher temperature range. The use of the proper calibrate temperature insures a good match in film density between the standard temperature source and the object being tested. The film densities were measured with a densitometer using an enlarger to project the image from the film to increase the area resolution. Calibrations were taken on each roll of film to account for any variations in film emulsion which may occur and in film development from roll to roll. The theory and operation of a similar system and a sample calculation of temperature readout are presented in reference 5.

For the wind-tunnel tests, calibrations were made by observing the calibrate source through the tunnel window and, in some cases, by observing the reflections off a mirror, whenever this procedure would be required to see the area of interest on the model. The window and mirror are, in effect, additional filters and must be included in the calibration of the working system. All calibrations were made in darkness to minimize errors due to extraneous light.

Emissivity

In order that the surface temperatures on the models be properly determined, the emissivity of the model material must be known. To determine the emissivity, tests were conducted on material samples for temperatures of 1500° F (1089° K) and 1800° F (1256° K) and over a wavelength range from 0.4 to 15 microns (the limits of the furnace used). The emissivity for the model material is shown in figure 5 over the wavelength range tested. The integrated emissivity over this range is here considered to be the total emissivity, which is the value required for computation of total heat radiation. The total emissivity, as determined from figure 5(a), is from approximately 0.90 to 0.95.

In determining the surface temperature with the use of the photographic pyrometer, a photographic emulsion is used to record the level of intensity. The characteristics of the film used are such that the energy is filtered over the visible portion of the spectrum, and the emissivity needed for photographic readout of temperature is the integrated value over this wave band. A plot of the emissivity over the visible spectrum from 0.4 to 0.8 micron is shown in figure 5(b). For the temperatures shown, the spectral emissivity is approximately constant and has an average value of about 0.66.

Errors and Limitations

In addition to the temperature limitations of the recording system, which depend on the characteristics of the film and filters used, there are other factors which affect the performance of the system. One of these factors is the effect of viewing angle between the camera line of sight and the local model surface. It was established that viewing angles up to 30° away from a normal to the surface could be accepted without incurring temperature errors greater than

about 1 percent at temperatures below 2500° F (1644° K). As a result, all data presented herein were obtained within this 30° angular limitation.

Another source of error for this technique arises from light emanating from a heated surface and reflecting from a cooler surface. The reflected light is seen by the pyrometer as surface temperature. The magnitude of error due to this effect was studied to a limited degree experimentally. The results of the study will be discussed in a later section of the paper.

Temperature error can result from an inaccuracy in the value of the surface emissivity. However, it was shown in reference 3 that an error of 25 percent in emissivity gives a temperature readout error of about 2 percent at 1600° F (1144° K). This minimized effect of the error is due to the rapid change in energy with temperature in the range of film sensitivity.

The general accuracy of the system for cases in which viewing was normal to the surface and no reflected light was present is indicated in figure 6. In this figure the surface temperatures of several stainless-steel configurations as afforded by the optical system are compared with the same surface temperatures as determined with thermocouples. There is generally good agreement between the two measurement methods. The absolute accuracy for a photometer system such as employed here is believed to be ± 4 percent, whereas the relative point-to-point accuracies over the surface are believed to be about ± 1 percent.

MODELS, APPARATUS, AND TEST PROCEDURES

Test Models

The models for the experimental evaluation of the present technique were fabricated in the manner previously described. The models tested included a blunted cone, several modifications of a boost-glide configuration, a hypersonic airplane configuration, and a blunt-faced reentry shape. These models will be referred to as models 1, 2, 3, and 4, respectively.

Model 1.- A sketch and photograph of model 1 is shown in figure 1. This blunted-cone model has a 10.2° half-angle and a nose radius of 0.25 inch (0.64 cm). The model is approximately 3.00 inches (7.62 cm) long and has a base diameter of 1.50 inches (3.81 cm).

Model 2.- The boost-glide models are approximately 2.8 inches (7.1 cm) long and have a maximum span of 2.19 inches (5.56 cm). Figure 2(a) is a three-view drawing of this configuration, along with several components incorporated in modifications of this model. This configuration had a spherical nose with a radius of 0.12 inch (0.30 cm) and a sweep back of 70° of the wing leading edge. The lower surface has a break with a 10° change in slope. The rear portion of the lower surface of the wing was used as a reference for angle-of-attack measurements. The four different modifications of this model that were tested will be designated as models 2A, 2B, 2C, and 2D; each of these models had side antenna fairings. Further description of these models appears in the following paragraphs.

Model 2A: Model 2A has surface gaps simulated by grooves milled in the surface of the model, as shown in figure 2(b). The grooves had widths of 0.025 and 0.050 inch (0.064 and 0.127 cm) and a depth of 0.025 inch (0.064 cm).

Model 2B: A photograph of model 2B is shown in figure 2(c). This model has a flow sensor extending out of the lower surface, and an attitude control flap extended 3° out of the surface.

Model 2C: Model 2C is the same as model 2B, except that the control flap is at -3° , or in a retracted position. The outline of the retracted flap can be seen in the drawing of figure 2(a). The bottom of this model was made smooth, and a portion of the lower surface was cut away to simulate the retracted flap.

Model 2D: Model 2D is the same as model 2C, with the addition of a recess in the bottom surface which is 0.30 inch (0.76 cm) long by 0.40 inch (1.02 cm) wide and is located just forward of the flow sensor. A photograph showing this recess in the model surface is presented in figure 2(d). The recess, which had a depth of 0.023 inch (0.058 cm), is also shown in figure 2(a).

Model 3.- A drawing of model 3 is shown in figure 3(a). This model has upper and lower vertical fins and a horizontal stabilizer with a negative dihedral of 15° . The model was 4.40 inches (11.18 cm) long, and it had a maximum span of 2.00 inches (5.08 cm). Figure 3(b) shows two views of the model.

Model 4.- Model 4 is a blunted-face reentry configuration having a maximum diameter of 1.50 inches (3.81 cm). A photograph and a sketch showing some pertinent dimensions of this model are shown in figure 4.

Apparatus

The 7-inch Mach 7 pilot tunnel at the Langley Research Center was used to conduct the present series of tests; it is a hypersonic blowdown facility which obtains a high-energy-level flow by burning methane in air under pressure. The products of combustion, which are formed from the burning process, are expanded through an axisymmetric nozzle and pass through the test section, where they are used as the test medium. This facility readily lends itself to the use of a photographic pyrometer for determining the surface temperatures since the tunnel test region simulates a high altitude and the absorption effect of the gas is minimized because of the low density. Photographs and a more complete description of this facility may be found in reference 6. Thermal and transport properties for the combustion products of methane and air have previously been determined and are presented in reference 7.

Procedure

The models tested were set approximately at the desired angle of attack with the use of angle-of-attack adapters. The actual angle, which was measured, varied slightly between configurations because of small errors in the alignment in the vertical plane of the support stud extending out of the back of the

model. The model was then rotated about a horizontal axis to expose the surface of interest to the photographic pyrometer.

For execution of the tests, the tunnel was started and allowed to reach the desired equilibrium conditions. The model was then inserted into the test section and allowed to heat for a period from 30 to 40 seconds. Pyrometer photographs were taken during this heating period at intervals which varied from 3 to 6 seconds.

The tests were conducted at a nominal Mach number of 7.0, and the data were obtained over a model-stagnation-point pressure range from approximately 5 to 17 psia (34 to 117 kN/m²) and for total temperatures which ranged from approximately 2700° F (1756° K) to 3180° F (2022° K). These conditions correspond to a free-stream Reynolds number of 0.44×10^6 and 1.58×10^6 per foot (1.44 and 5.19 per μm), respectively. As with the pyrometer calibration, the tests were performed in darkness to eliminate possible effects of extraneous light.

DATA REDUCTION AND ACCURACY

The densitometer used for determining relative density at specific locations on the model image had an orifice diameter of 0.10 inch (0.254 cm). The image of the model was projected onto a screen and was about four times the size of the model. This enlargement permitted temperatures to be read at locations on the model as close as 0.025 inch (0.064 cm) apart, if desired, without overlapping any of the previous area under measurement. To obtain the temperature contours, the required film densities to give specific surface temperatures were computed for each lens. The film was then scanned to locate the required densities and the isotherm contours were then plotted.

Typical variations of measured surface temperature with time for three locations on the bottom surface of model 2 are presented for an angle of attack of 30° in figure 7. The local temperature is made nondimensional by dividing by the stagnation temperature. The rate of temperature rise after 30 seconds approaches zero for each of the locations considered. The temperature-ratio level, however, is still 5 to 10 percent below the computed equilibrium value. This discrepancy is largely due to the fact that conduction, although very low as a result of the material used for the model fabrication, still accounts for a significant portion of the aerodynamic heat input. Since temperatures on the surface are somewhat below the actual equilibrium temperature which would exist without internal heat conduction, calculating the local heating rate directly from the measured local temperature can result in errors as large as 15 to 35 percent if the effect of internal heat conduction is neglected, as is done in equation (1). For the order of these errors to be reduced, the heating rates, when presented, are in ratio form when the temperature in the denominator (see eq. (3)) is also a measured quantity. By use of temperature ratios, the possible error in the relative heating is reduced to within about ± 10 percent, which is considered to be an acceptable overall accuracy for this technique.

RESULTS AND DISCUSSION

The wind-tunnel experiments which were performed were made basically to determine the degree and the extent to which the aerodynamic heating could be studied by using the described technique. Hence, the technique was applied to define the isotherm patterns over a number of bodies heated by a hypersonic stream. As shown previously in the section entitled "General Description of Technique," isotherms are essentially lines of constant heating rate; therefore, isotherm patterns may be considered to be heating patterns. The heating rates over the surface of the model are dependent upon the tunnel stagnation pressure and temperature. Inasmuch as the stagnation conditions of the tunnel were not controllable to the degree necessary to permit the assumption of identical stagnation-point heating between test runs, the comparison of the surface position of a discrete isotherm for different tests to ascertain changes in heating was not possible. Although this problem could have been alleviated by transforming the isotherms to lines of constant heating-rate ratio, such effort was not believed justified inasmuch as the detailed patterns would not be changed by the transformation. Hence, the bulk of the data is presented as temperature contours over the surface of the model with the discussion limited to the pattern changes. When comparisons are made with other data, comparison curves are shown in the form of nondimensional heating-rate ratio.

Blunted-cone model (model 1).- The blunted-cone model was geometrically the simplest body shape tested. The nondimensional heating patterns over the profile views of model 1 at various angles of attack are presented in figure 8. The heating-rate ratio presented is referenced to the theoretical stagnation-point heating rate computed from tunnel reference conditions. The use of the theoretical value of heating rate as the reference quantity was necessitated here as a result of the inability to locate the optical pyrometer to view the stagnation region properly. Note that the isotherm patterns were terminated at a position corresponding to a viewing angle of 30° for reasons of accuracy as previously discussed. Also included in the figure is a bottom view of the model at an angle of attack of 22° as taken with the high-temperature filters (minimum temperature was approximately 1900° F (1311° K)). This view is provided to show how the isotherm patterns close at the bottom center line of the cone inasmuch as this information could not be obtained accurately from the side view due to the large viewing angle in this region.

The patterns show the increased heating on the windward side of the cone as the angle of attack is increased. The trend of heating with angle of attack is as would be expected. It is indicated that the present technique is capable of defining the relative nondimensional heating-rate contours within acceptable limits.

Boost-glide models (model 2).- Isotherms for the boost-glide models are presented in figures 9 to 13. These models were tested at two stagnation-point pressure levels corresponding to free-stream Reynolds numbers of approximately 0.5×10^6 and 1.5×10^6 per foot (1.64 and 4.91 per μ m). Figure 9(a) shows isotherm contours on the lower wing surface of model 2A at several angles of attack. It can be seen from this figure that the grooves cut in the surface

disrupted the boundary-layer buildup on the wing surface and caused discontinuities in the isotherms at the grooves.

In the side views of the isotherm patterns of figure 9(b) the discontinuities in isotherms are noted along the leading edge. Also to be noted for the positive angles of attack are results of discrete disturbances apparently originating at the grooves and washing the sides of the fuselage. The resulting hot spots appear to vary in shape and location as the angle of attack is changed.

The effect of adding the flow sensor and attitude control flap (model 2B) on the isotherm patterns of the lower wing surface are indicated in figures 10(a) and 10(b). Note the evidence of increased heating in the vicinity of the flow sensor and the distortions of the isotherm pattern resulting from the shock originating at the flow sensor and from the flow-sensor wake. The observed distortions become more severe as the angle of attack is increased. At angles of attack near 20° for the high Reynolds number condition (fig. 10(b)), the effect of the presence of the flow sensor is evident over the attitude control flap and affords a very uneven heating to its surface. It should be mentioned that an error exists in the magnitude of the isotherms near the flow sensor. This error, as previously mentioned, arises from the fact that light emanating from the flow sensor is reflected from the bottom of the model and is seen by the pyrometer as heat.

An experimental check was made to determine the apparent surface temperature increase due to the reflected light. For the check, model 2 was modified to incorporate a silica probe, as indicated by the sketch in figure 14. The spherical tip of the probe was small (0.06-inch (0.15-cm) radius) and was located well forward of the support such that its bow shock wave impinged on the lower wing surface aft of the area to be studied. Because the spherical tip of the probe was small, it became quite hot when subjected to the aerodynamic heating afforded by the tunnel test conditions. The light emanating from the hot probe tip reflected from the flat lower wing surface and was observed as heat by the photometer. The apparent surface temperature indicated by the photographic-pyrometer measurements were compared with similar measurements made without the probe. The ratio of the difference in temperatures to the temperature without reflected light is presented as a function of model surface temperature in figure 14 for a number of surface locations relative to the edge of the probe. For the low angles of attack, the surface temperature was obtained from theory since the temperatures over the lower surface were too low to be sensed by the photographic pyrometer. It is indicated that for a surface temperature as low as 1500° R (833° K) the reflected light could produce an error in temperature reading as large as about 35 percent. The error becomes smaller as the point considered gets further away from the light source. More important is the evidence that as the surface heats to temperatures that are measurable with the photometer the error drops below 10 percent. Reductions of the surface reflectivity by use of a dull black paint on the surfaces reduced the magnitude of the error produced by reflected light. It was indicated that at a horizontal distance of 0.2 inch (0.5 cm) from the probe tip the maximum error was reduced to about 10 percent by use of the black paint. Other materials to reduce reflectivity may offer greater reductions.

The isotherm patterns on the side views of model 2B (fig. 10(c)) display the effects of angle-of-attack changes on the heating of the side of the model. At angles of attack of 9.3° and 18.0° there is evidence of a disturbance (probably a vortex) originating at the juncture of the wing leading edge and the body and washing the body. The resulting region of increased heating appears to be greatly reduced at an angle of attack of 28.7° indicating that the flow is being deflected away from the upper surface at this attitude.

Retracting the attitude control flap inward 3° (model 2C), resulted in a noticeable change in the isotherm pattern on the flap for the higher angles of attack. (See fig. 11.) In comparing the isotherms for angles of attack of 20.0° and 29.8° for model 2C (fig. 11) with the isotherms for angles of attack of 19.1° and 29.0° for model 2B (fig. 10(b)), it is noted that the outwardly deflected flap results in isotherm patterns greatly different from those for the inwardly deflected flap. From the characteristics of the isotherm patterns, this difference apparently resulted from a combination of the flow-sensor shock-wave interaction with the extended flap surface. For the retracted flap, only the flow-sensor wake appears prominent in the isotherm pattern. Also shown in figure 11 are isotherms for model 2C at an angle of attack of 20.0° and a yaw angle of 5.9° . Comparison of the conditions with and without yaw in this figure reveals the change in isotherm pattern resulting from yaw. The principal result noted is a shift in pattern with greater heating occurring on the windward leading edge than on the leeward leading edge; this shift in pattern is a result of the effective decrease in leading-edge sweepback angle.

Figure 12 presents isotherms on the lower wing surface of model 2D. This model is model 2C with a rectangular cavity in the surface ahead of the flow sensor. It was tested to indicate the effect of the cavity on the heating of the wing surface. As is indicated, the rearward edge of the cavity received severe heating from flow impingement. The resulting shock-wave—surface interaction caused a strip of intense heating on each side of the flow sensor and the area bounded by these strips was generally hotter than for the cases without the cavity.

Figure 13 presents isotherms for the upper surface of model 2 at negative angles of attack for the test conditions at the higher Reynolds number. It is indicated by this figure that at a low angle of attack the upper surfaces of the wing-body experiences heating equal to, if not exceeding, that of the lower wing surface. As the angle of attack becomes more negative, the patterns indicate that the heating becomes more severe. The asymmetry of the patterns on the upper body surface results from an asymmetry of body shape rather than from a peculiar flow pattern. The particular body tested was found to have a slight depression on one side near the top of the body. This asymmetry resulted in the difference in isotherm position on the two sides of the body.

Schlieren photographs taken of model 2 are presented in figure 15 for angles of attack from -1.0° to 31.0° and for free-stream Reynolds numbers of approximately 0.5×10^6 and 1.5×10^6 per foot (1.64 and 4.91 per μm). As a result of the lack of sensitivity of the schlieren system used, only the major shock waves are clearly discernible. Hence, no significant effects of Reynolds number could be noted. It was noted, however, that the bow wave of the flow

sensor interacted with the main wing-body shock wave at angles of attack greater than 11.2° . This interaction may have had a pronounced effect on the resulting heating-pattern changes due to the presence of the flow sensor.

To afford an insight to the repeatability of the data and to the degree to which the present results agree with theory, plots of heating-rate ratio as a function of nondimensional distance along the wing center line on model 2 are presented in figure 16. For this figure the local center-line heating rate, made nondimensional by dividing by the heating rate at station $x/x_0 = 0.285$, is plotted as a function of the distance from the apex of the wing planform to the break in wing surface, as indicated by the sketch in the figure. The solid curves in the figure represent strip theory for laminar flow predicting the heating along the wing center line.

In general, the repeatability of data is seen to be good. Furthermore, good agreement between experiment and theory is indicated for angles of attack up to about 20° . The crossing of the theoretical curve by the experimental data at $\alpha = 10^\circ$ and 20° is believed to result largely from the increased heating caused by the interaction of the lower surface boundary layer and the shock wave from the flow sensor. The increased heating at the higher angles for model 2A, which had no flow sensor, was believed to be induced by the sharp edges along the grooves in the lower surface. At an angle of attack near 30° (which corresponds to an angle of attack of 40° on the surface being studied), three-dimensional effects apparently cause a significant increase in the center-line heating over the rearward portion of the wing surface.

It is also noted that there is no significant Reynolds number effect on the center-line heating distribution of model 2B for the angle-of-attack range covered. This result is probably as would be expected inasmuch as the heating distributions shown are ahead of the disturbances and boundary-layer transition did not occur on the surface for the Reynolds number range investigated.

Spanwise heating distributions for model 2B are presented in figure 17. In this figure the local heating rate is made nondimensional by dividing by the heating rate at the center line for that particular longitudinal station. The data are presented primarily to indicate that the spanwise distributions of heating are as would be expected. Here again, the portion of the wing surface from which data are presented is ahead of the flow sensor. Inasmuch as the center-line heating rate \dot{q}_c changes with both angle of attack and longitudinal station, the change in spanwise distribution often results from a change in center-line heating rate. This change is particularly true for figure 17(b) in which it is indicated that the distribution at station $x/x_0 = 0.4$ tends to flatten at the higher angles of attack. In this case the flattening results solely from an increase in center-line heating rather than a reduction of out-board heating.

Hypersonic airplane (model 3).- Isotherms measured for the surfaces of the hypersonic airplane configuration are presented in figure 18. Data are presented for a free-stream Reynolds number of 0.75×10^6 per foot (2.46 per μm) and for angles of attack of 0° and 15° . At zero angle of attack the isotherms on the upper and lower surfaces of the wing are orderly and approximately

parallel to the wing leading edge. The horizontal stabilizer, however, experiences a nonuniform flow field as a result of being in the wake of the wing. Note the hot spots near the tips of the stabilizer. Increasing the angle of attack to 15° places the stabilizer in a more uniform flow, and as a consequence its leading edge undergoes a more uniform heating. The lower surface of the wing at this angle of attack, however, showed considerable distortions in the isotherm patterns. A typical schlieren photograph of model 3 is shown in figure 19. Upon examination of several schlieren photographs of the flow field around this model, it was found that these observed irregularities resulted from the interaction of the shock waves from the model nose and side fairings with those of the wing surface. The waves cross the wing surface in the regions where the isotherms indicated increased heating.

The isotherms on the side of model 3 (fig. 18(b)) indicate that at low angles of attack the pilot canopy and upper fin receive considerable heating. At the higher angle of attack the canopy is not heated as severely as a result of being shielded from stream impingement, and the upper fin received significant heating only at its tip leading edge.

Blunt-faced reentry body (model 4).- The heating distribution for model 4 (fig. 4) is presented in figure 20. Presented is the ratio of the local heating rate to the stagnation-point value as a function of nondimensional surface distance. Distributions are presented for angles of attack of 0° and $\pm 5^\circ$ as measured at a free-stream Reynolds number of 0.9×10^6 per foot (2.95 per μm). The heating is seen to increase as the model corner, which is of small radius, is approached and then drops rapidly along the edge of the model. The heating rate is highest for an angle of attack of 5° . These heating distributions showing an increase in heating near the corner are typical of those experienced for flat-faced bodies.

CONCLUDING REMARKS

A technique has been described and demonstrated whereby equilibrium isotherm patterns or heating-rate distributions over the surface of a model immersed in a hypersonic stream can be measured relatively easily for a wide range of model geometries. The technique involves subjecting a slip-cast fused silica model to the aerodynamic heating of the stream and measuring the resulting heating distributions with a photographic pyrometer. Because of the characteristics of the silica, the model surface rapidly approaches its equilibrium temperature. Experimental results from the technique are presented which indicate the detail with which the temperature distributions and the aerodynamic heating patterns can be defined and the variation in heating patterns that can result from the addition of appendages to or the change in attitude of hypersonic vehicle shapes.

In general, it was indicated that the technique will provide a correct indication of the aerodynamic heating distributions over models immersed in a hypersonic stream. Furthermore, the data are obtainable rapidly and without excessive cost.

Langley Research Center,
National Aeronautics and Space Administration,
Langley Station, Hampton, Va., December 17, 1964.

REFERENCES

1. Stainback, P. Calvin: A Visual Technique for Determining Qualitative Aerodynamic Heating Rates on Complex Configurations. NASA TN D-385, 1960.
2. Lorenz, George C.; Sartell, Robert J.; and Strack, Sainsbury L.: Experimental Investigation of Heat Transfer to Complex Aerodynamic Configurations at Hypersonic Speeds. ASD-TDR-63-530, U.S. Air Force, Sept. 1963.
3. Siviter, James H., Jr.; and Strass, H. Kurt: An Investigation of a Photographic Technique of Measuring High Surface Temperatures. NASA TN D-617, 1960.
4. Mechtly, E. A.: The International System of Units - Physical Constants and Conversion Factors. NASA SP-7012, 1964.
5. Exton, Reginald J.: Theory and Operation of a Variable Exposure Photographic Pyrometer Over the Temperature Range 1800° to 3600° F (1255° to 2255° K). NASA TN D-2660, 1965.
6. Weinstein, Irving: Heat Transfer and Pressure Distributions on a Hemisphere-Cylinder and a Bluff-Afterbody Model in Methane-Air Combustion Products and in Air. NASA TN D-1503, 1962.
7. Leyhe, E. W.; and Howell, R. R.: Calculation Procedure for Thermodynamic, Transport, and Flow Properties of the Combustion Products of a Hydrocarbon Fuel Mixture Burned in Air With Results for Ethylene-Air and Methane-Air Mixtures. NASA TN D-914, 1962.

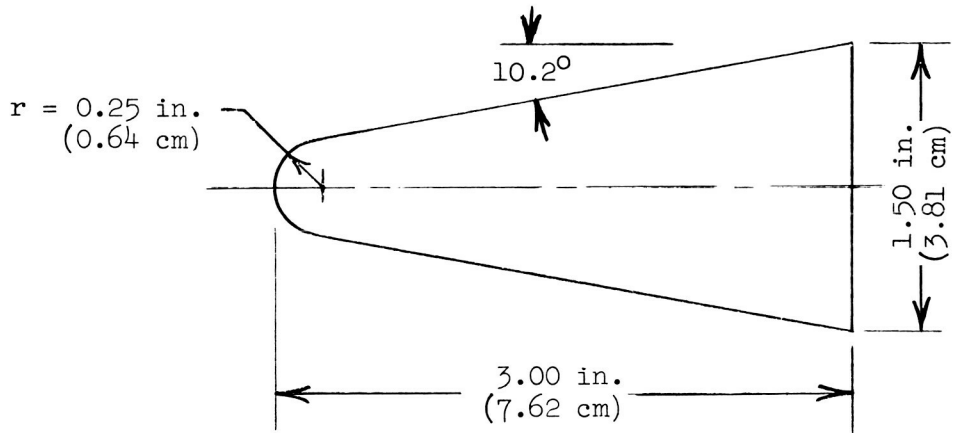
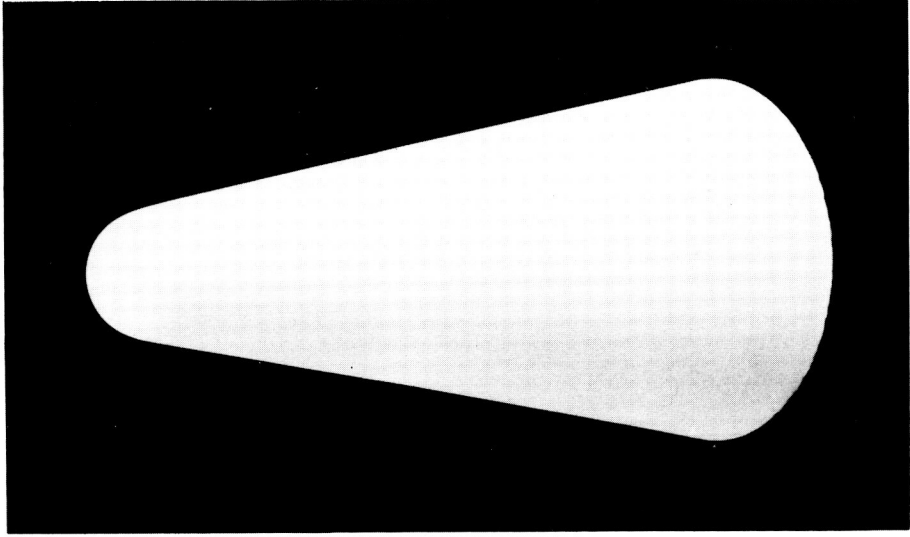
TABLE I.- PROPERTIES OF CERAMIC MATERIAL

(a) General properties

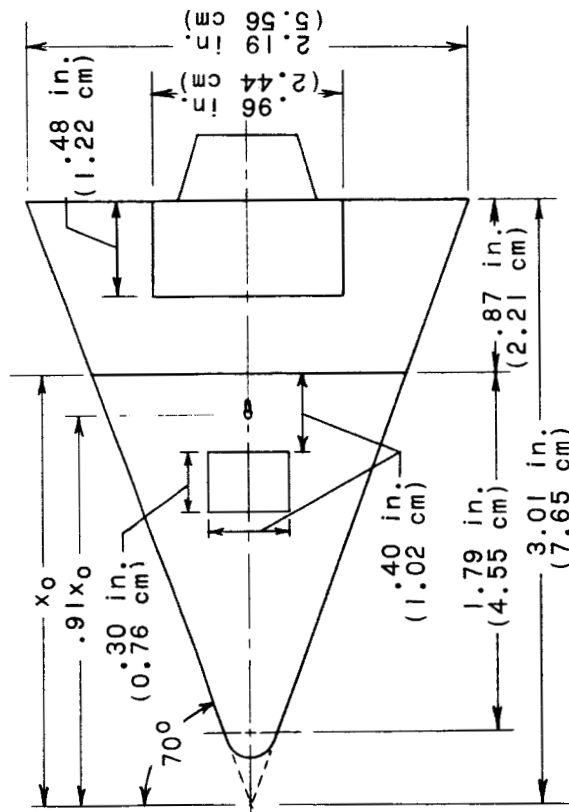
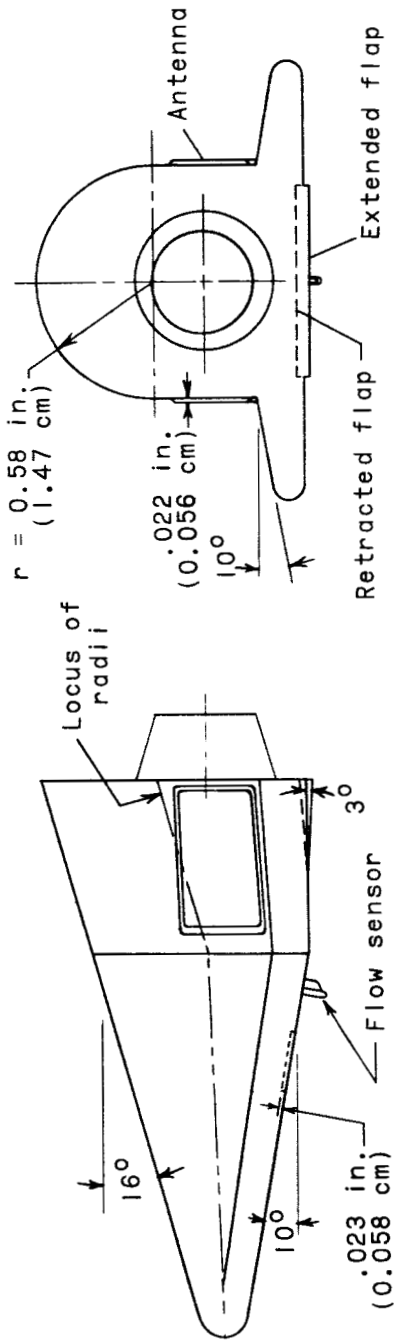
Composition: fused silica (major impurity is Al_2O_3), percent 99.8
 Density, lb/ft³ (kg/m³) 115 (1840)
 Color White
 Luster Matte
 Linear expansion from 0° C to 1000° C, per °C 0.54×10^{-6}
 Tensile strength, psi (MN/m²) 1000 to 2000 (6.9 to 13.8)
 Compressive strength, psi (MN/m²) over 20 000 (138)

(b) Thermal properties

Mean temperature		Specific heat		Thermal conductivity	
°F	°K	Btu/lb-°F	J/g-°K	Btu/ft ² -hr-°F/in.	W/m-°K
300	422	0.223	0.933	2.25	0.324
500	533	.244	1.021	3.00	.432
800	700	.260	1.088	3.80	.548
1000	811	.265	1.109	4.00	.577
1300	978	.283	1.184	4.32	.623
1600	1144	.285	1.192	5.40	.778
1800	1256	.293	1.226	6.84	.986
2000	1367	.298	1.247	7.80	1.124

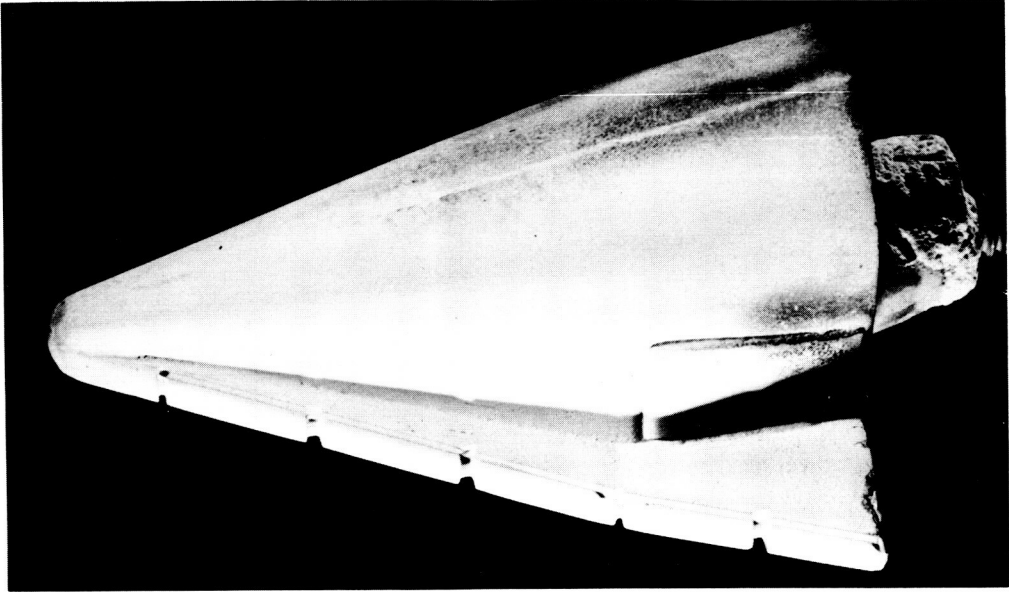


L-62-8533.1
Figure 1.- Photograph and sketch of blunted-cone model (model 1).

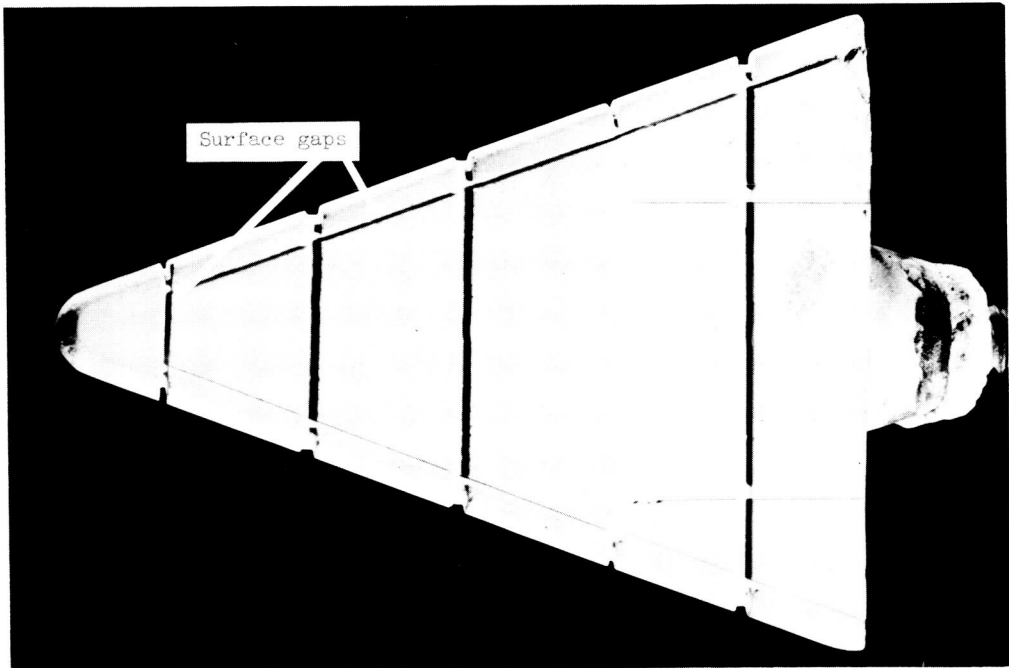


(a) Drawing illustrating modifications of model 2.

Figure 2.- Drawing and photographs of modifications of boost-glide model (model 2).



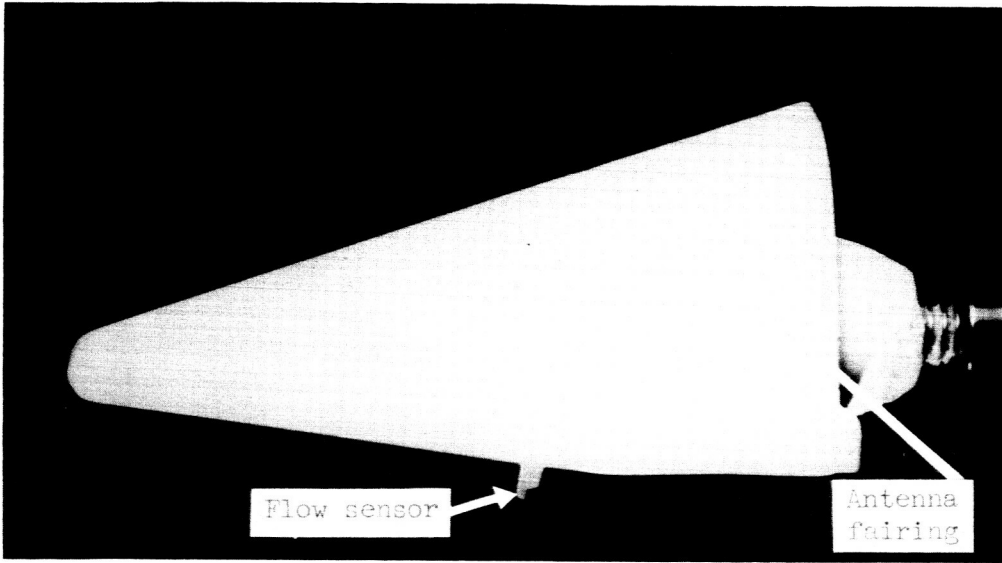
L-63-4406



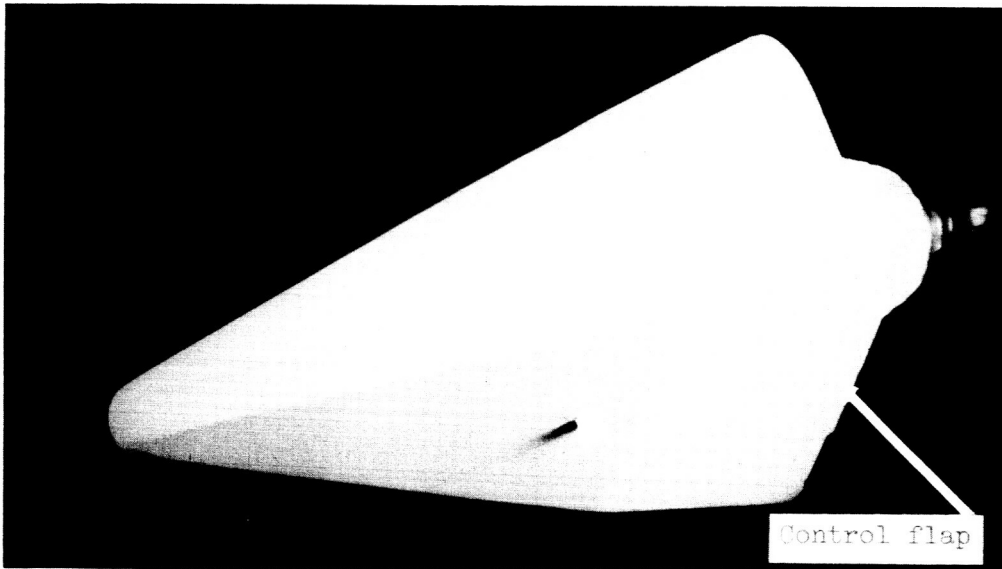
(b) Photographs of model 2A.

L-63-4407.1

Figure 2.- Continued.



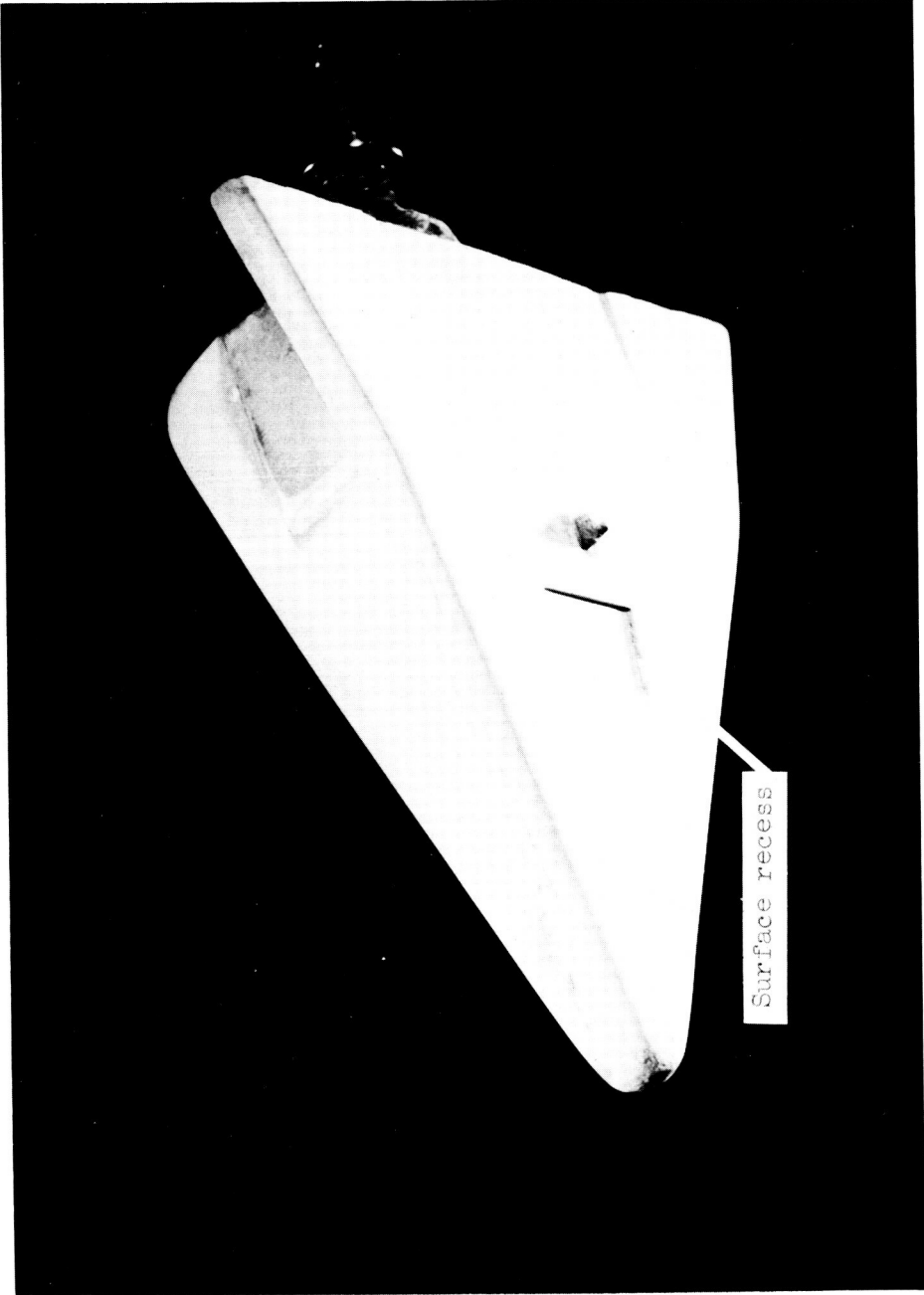
L-62-9498.1



(c) Photographs of model 2B.

L-62-9497.1

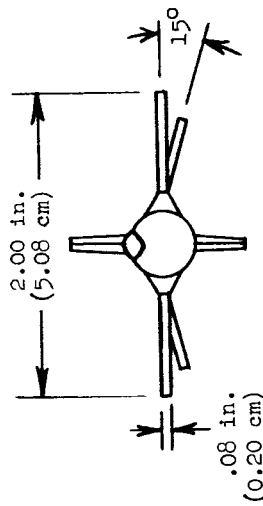
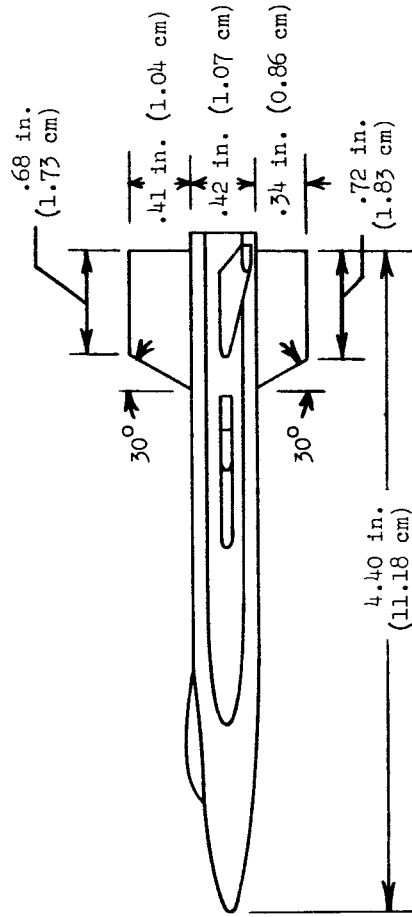
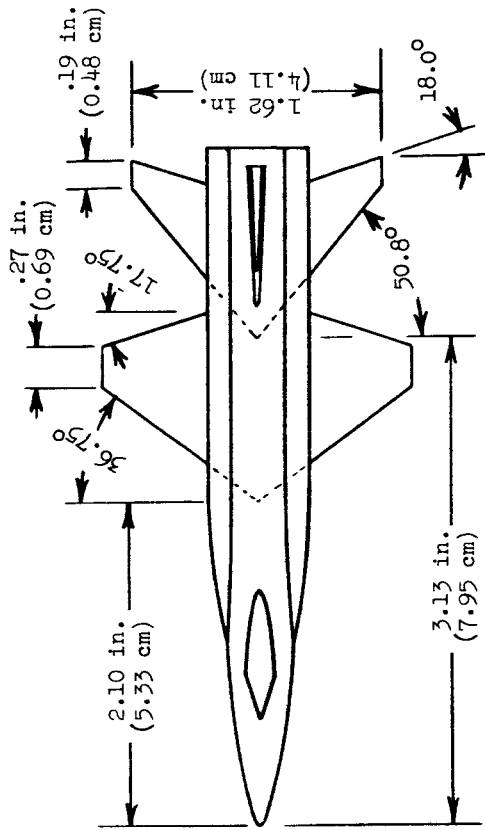
Figure 2.- Continued.



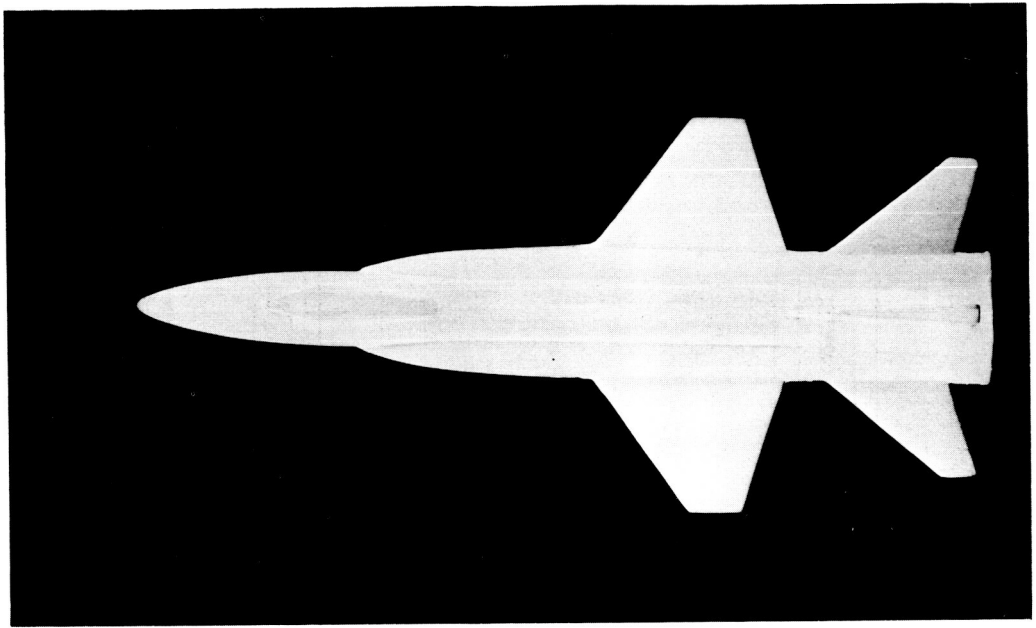
I-63-4404.1

(d) Photograph of model 2D.

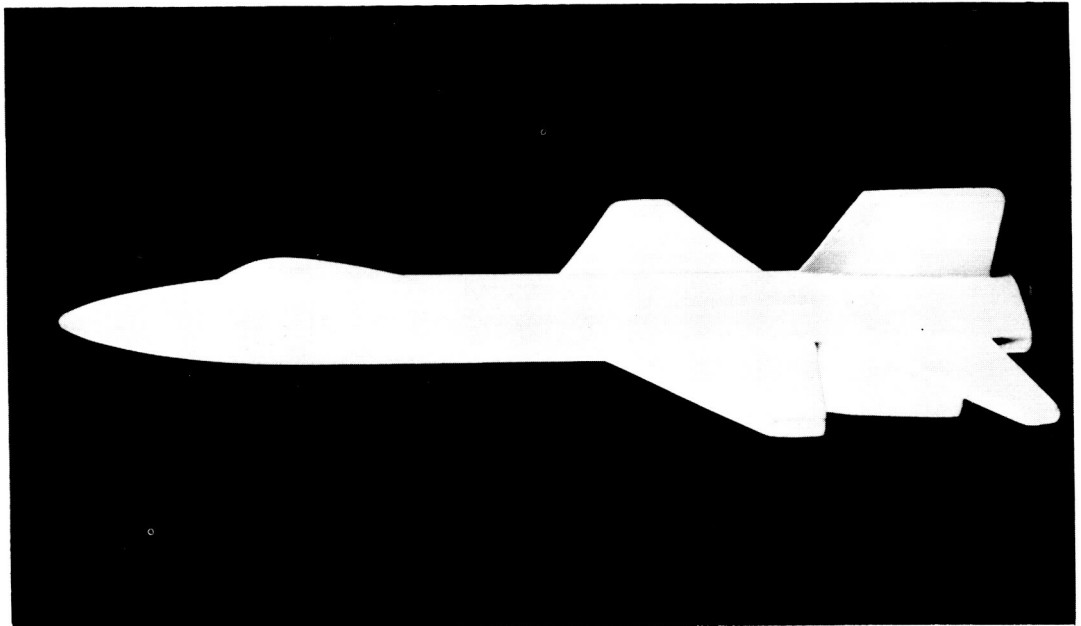
Figure 2.- Concluded.



(a) Pertinent details of model 3.
 Figure 3.- Hypersonic airplane configuration (model 3).



L-63-6313



(b) Photographs of model 3.

L-63-6314

Figure 3.- Concluded.

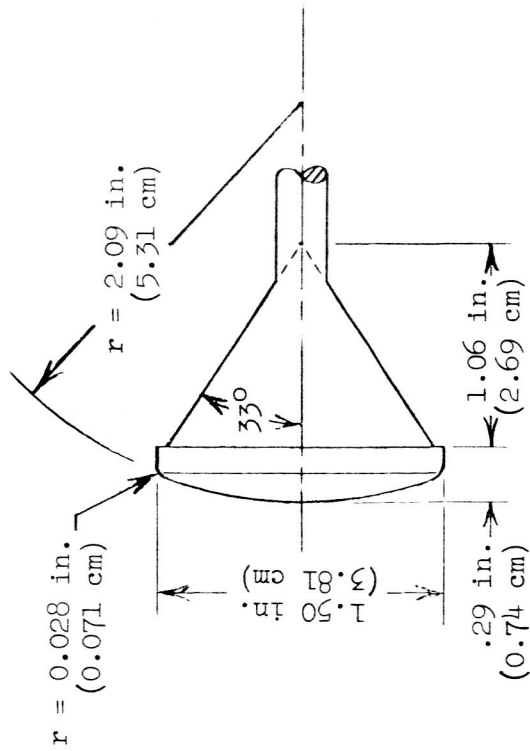
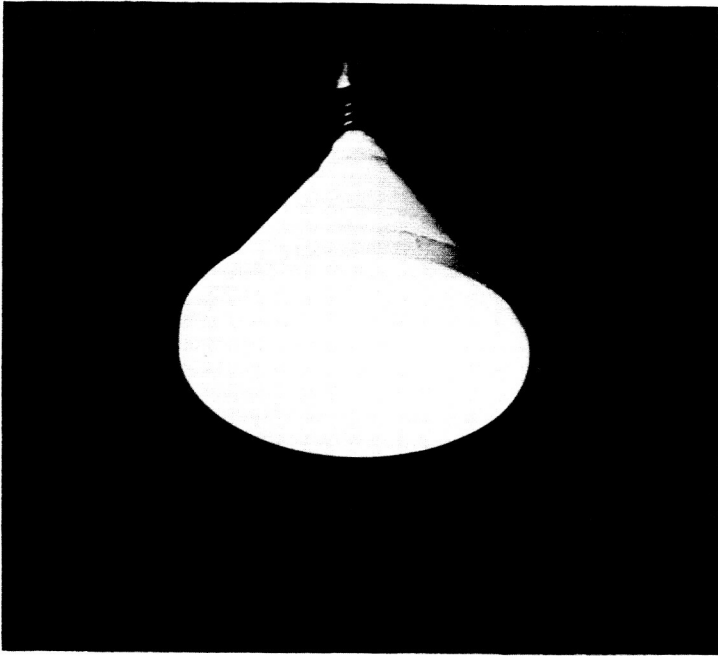
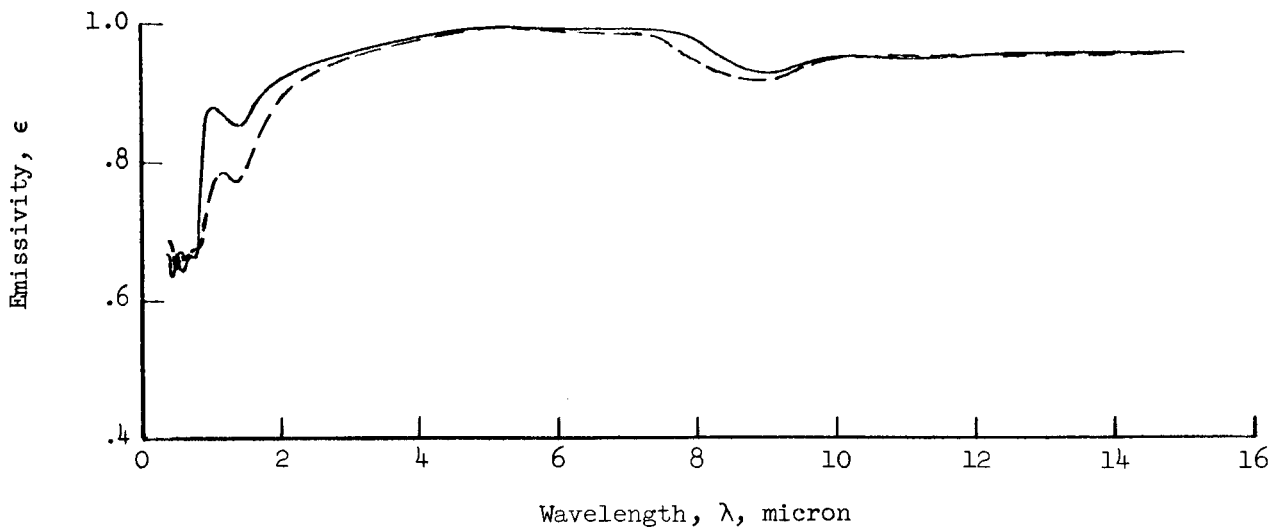
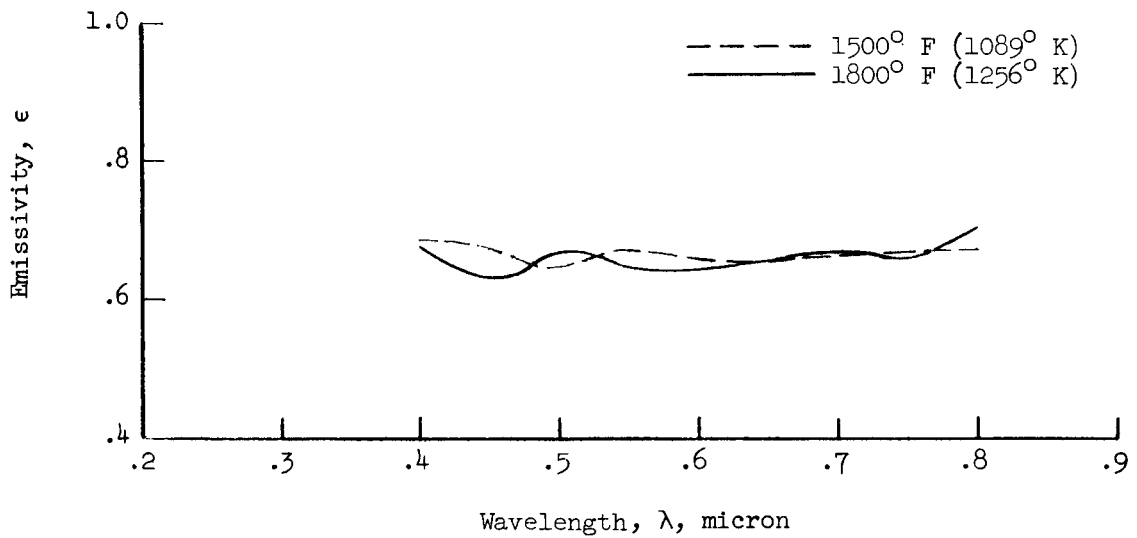


Figure 4.- Photograph and sketch of blunt-faced reentry model (model 4).

L-62-8535.1



(a) Total emissivity.



(b) Emissivity over visible wavelength.

Figure 5.- Variation of emissivity with wavelength for ceramic material.

- Semicylinder
 - ◇ Hemisphere-cylinder
 - △ Flat strip, electrically heated
 - Line of equality
- } Aerodynamically heated

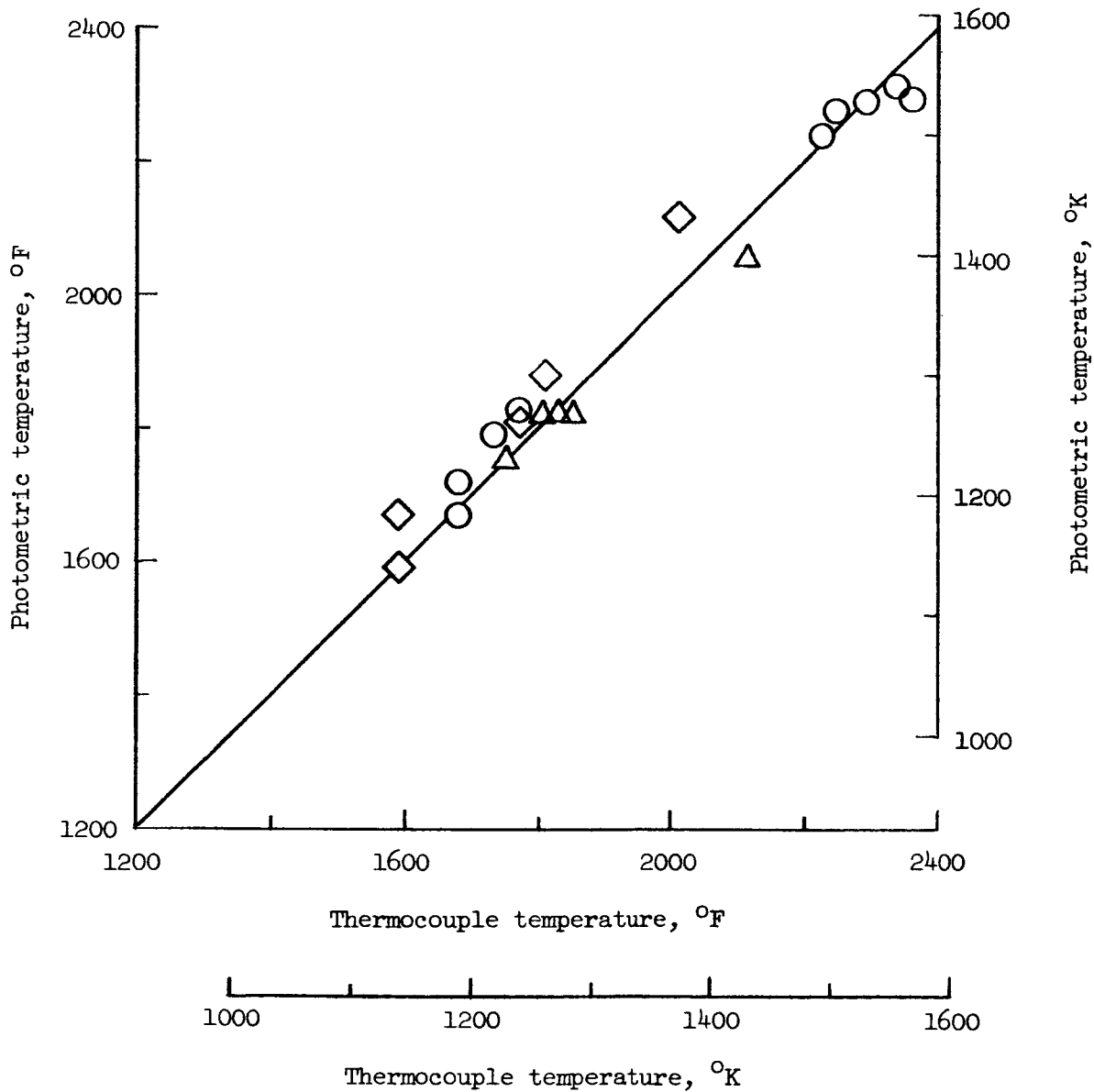


Figure 6.- Comparison of surface temperatures as indicated by photographic pyrometer with those indicated by thermocouples. (These samples were constructed of stainless steel; $\epsilon = 0.30$.)

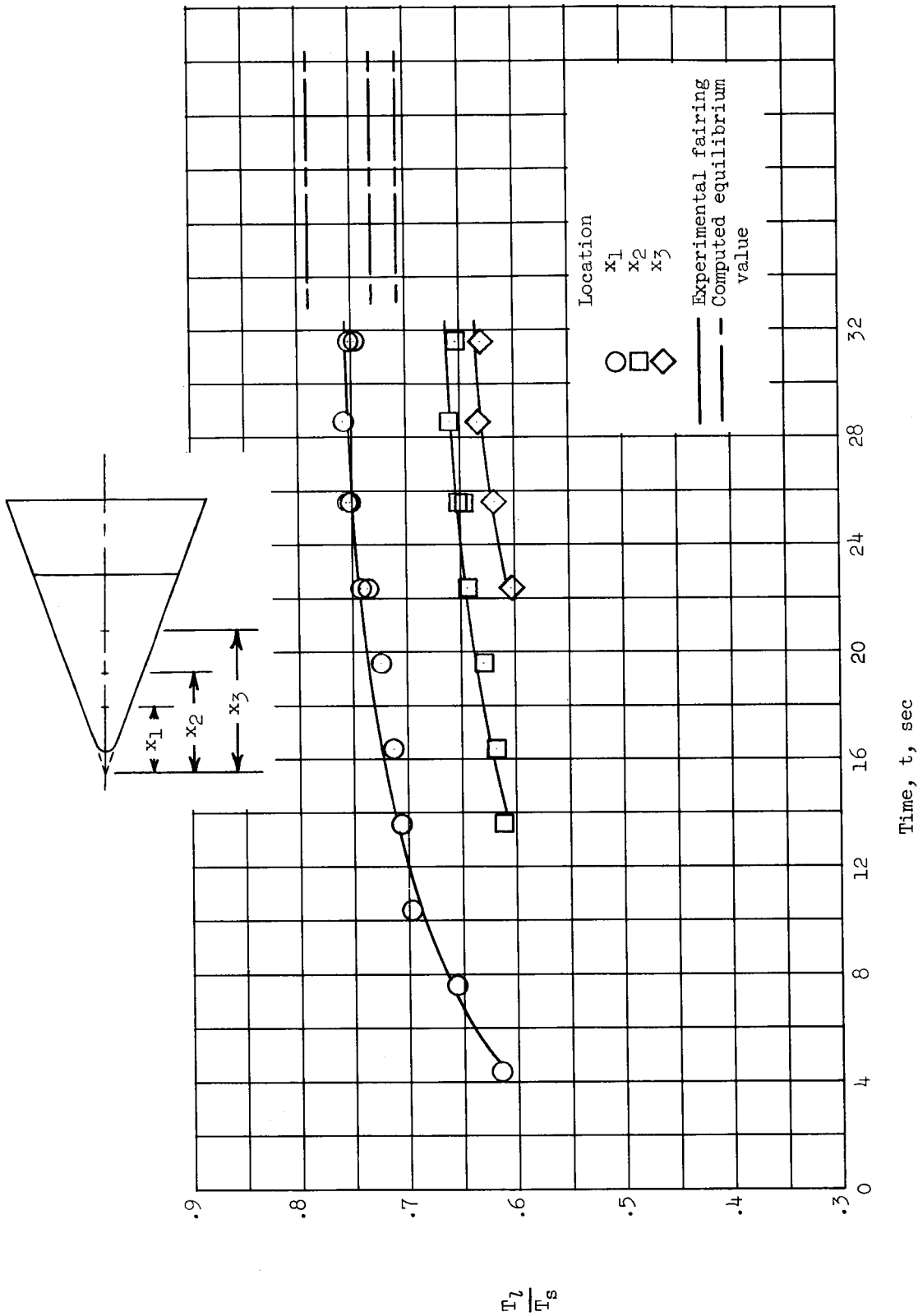
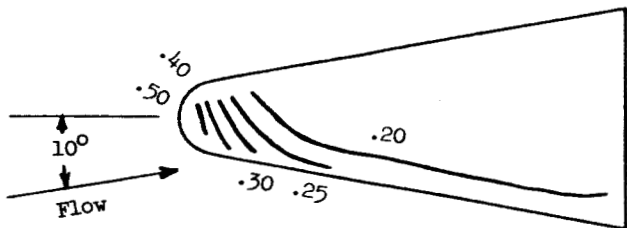
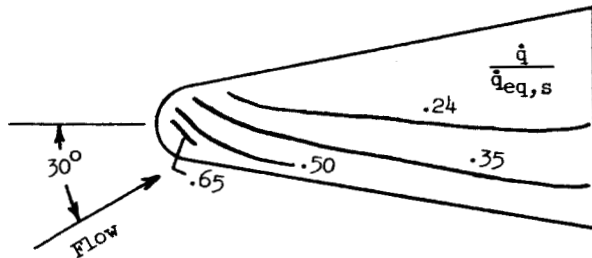


Figure 7.- Variation of surface temperature with time showing approach to equilibrium surface conditions for model 2. $\alpha = 30^\circ$.

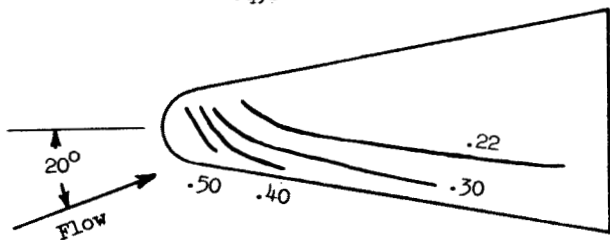
Side view
 $T_t = 3000^\circ \text{ F} (1922^\circ \text{ K})$
 $T_{eq,s} = 2610^\circ \text{ F} (1706^\circ \text{ K})$



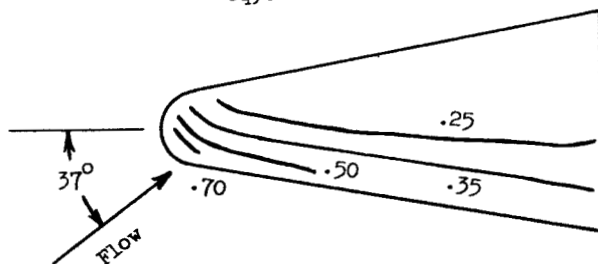
Side view
 $T_t = 2840^\circ \text{ F} (1833^\circ \text{ K})$
 $T_{eq,s} = 2490^\circ \text{ F} (1639^\circ \text{ K})$



Side view
 $T_t = 2920^\circ \text{ F} (1878^\circ \text{ K})$
 $T_{eq,s} = 2545^\circ \text{ F} (1669^\circ \text{ K})$



Side view
 $T_t = 2770^\circ \text{ F} (1794^\circ \text{ K})$
 $T_{eq,s} = 2435^\circ \text{ F} (1608^\circ \text{ K})$



Bottom view
 $T_t = 2800^\circ \text{ F} (1811^\circ \text{ K})$
 $T_{eq,s} = 2460^\circ \text{ F} (1622^\circ \text{ K})$

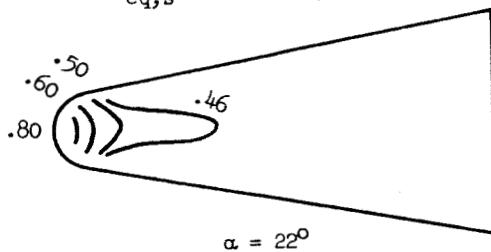
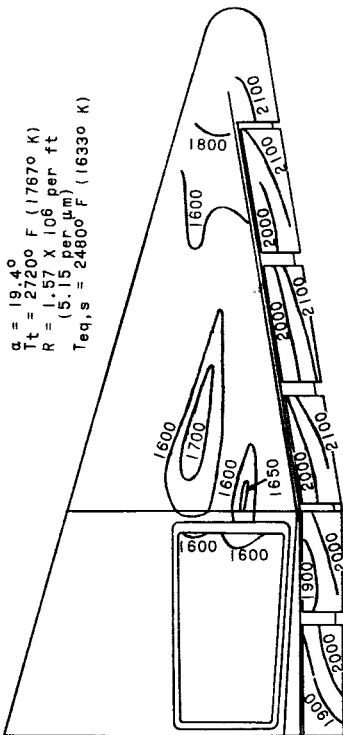


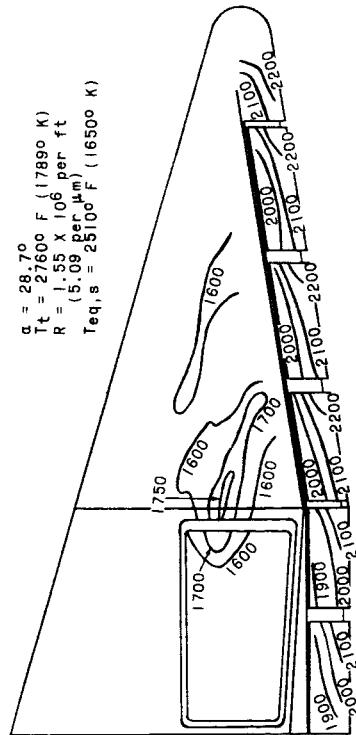
Figure 8.- Nondimensional heating rates over surfaces of model 1.

$$R \approx 1.5 \times 10^6 \text{ per foot (4.9 per } \mu\text{m)}.$$

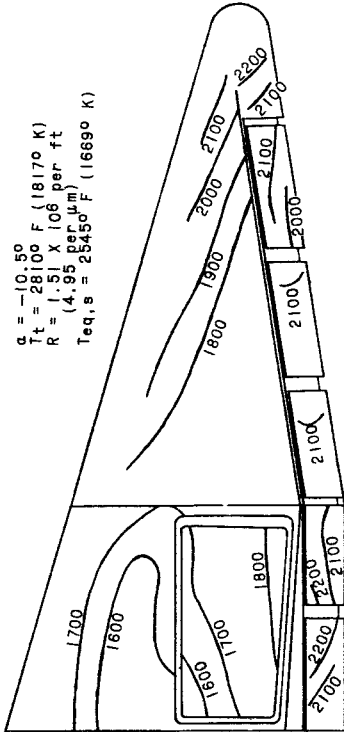


$\alpha = 19.40$
 $T_t = 2720^\circ \text{F} (1787^\circ \text{K})$
 $R = 1.57 \times 10^6 \text{ per ft}$
 $(5.15 \text{ per } \mu\text{m})$
 $T_{eq,s} = 2480^\circ \text{F} (1633^\circ \text{K})$

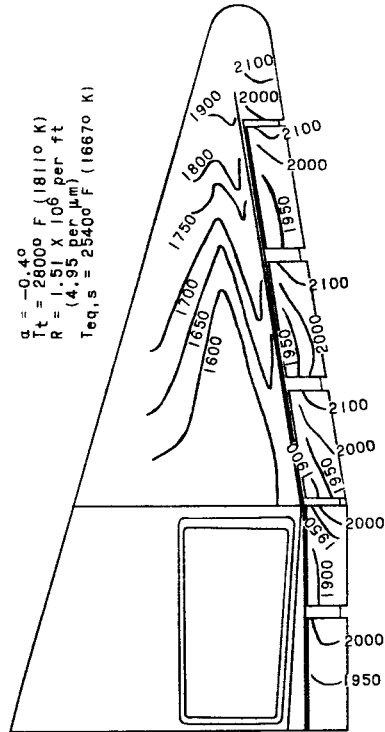
Temperature of	ok
1600	1144
1650	1172
1700	1200
1750	1228
1800	1256
1900	1311
1950	1339
2000	1367
2100	1422
2200	1478



$\alpha = 28.70$
 $T_t = 2760^\circ \text{F} (1789^\circ \text{K})$
 $R = 1.55 \times 10^6 \text{ per ft}$
 $(5.09 \text{ per } \mu\text{m})$
 $T_{eq,s} = 2510^\circ \text{F} (1650^\circ \text{K})$



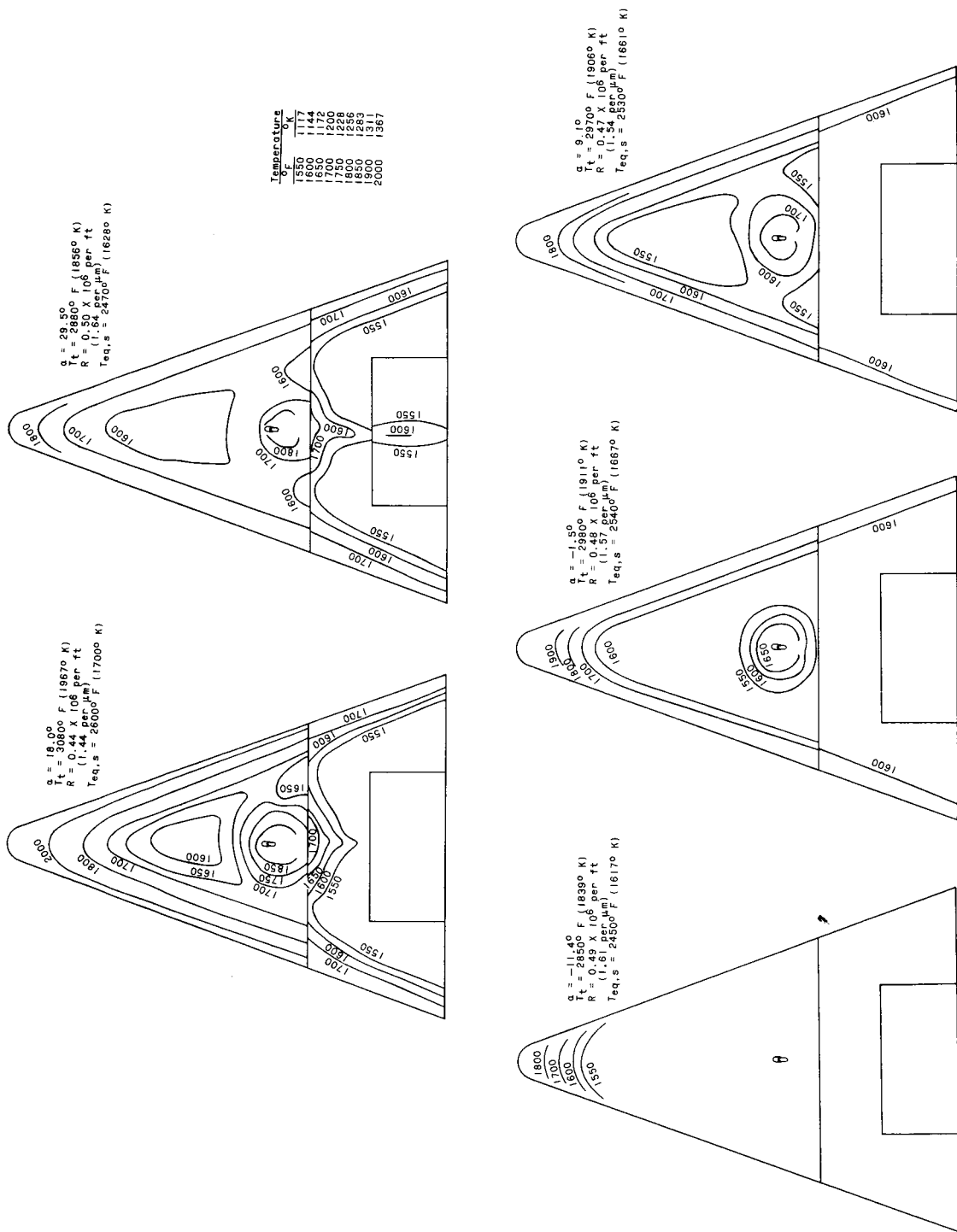
$\alpha = -10.50$
 $T_t = 2810^\circ \text{F} (1817^\circ \text{K})$
 $R = 1.51 \times 10^6 \text{ per ft}$
 $(4.95 \text{ per } \mu\text{m})$
 $T_{eq,s} = 2545^\circ \text{F} (1669^\circ \text{K})$



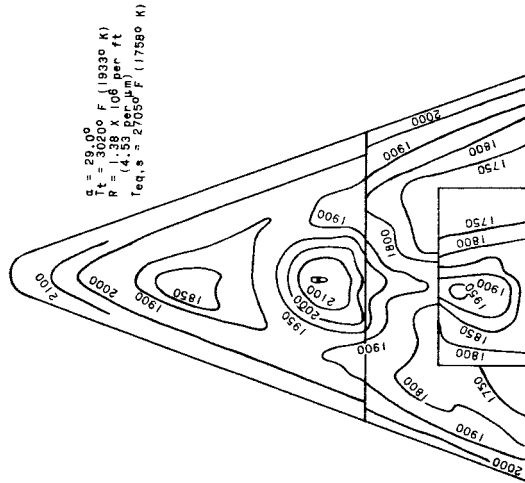
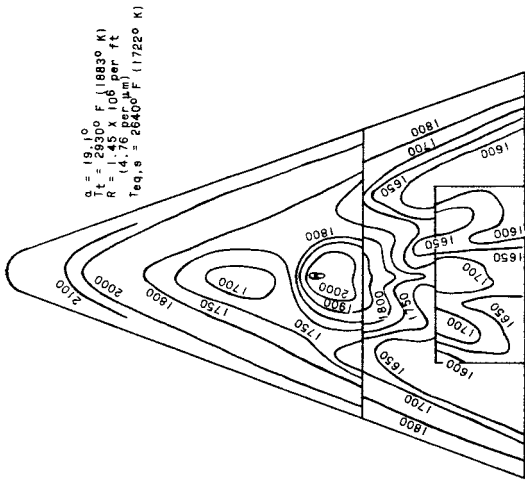
$\alpha = -0.40$
 $T_t = 2800^\circ \text{F} (1811^\circ \text{K})$
 $R = 1.51 \times 10^6 \text{ per ft}$
 $(4.95 \text{ per } \mu\text{m})$
 $T_{eq,s} = 2340^\circ \text{F} (1667^\circ \text{K})$

(b) Side views.

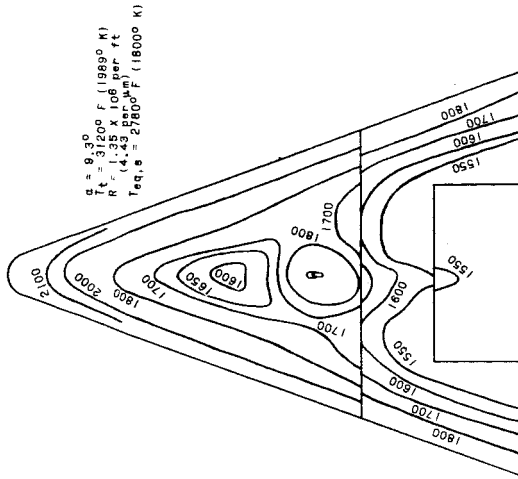
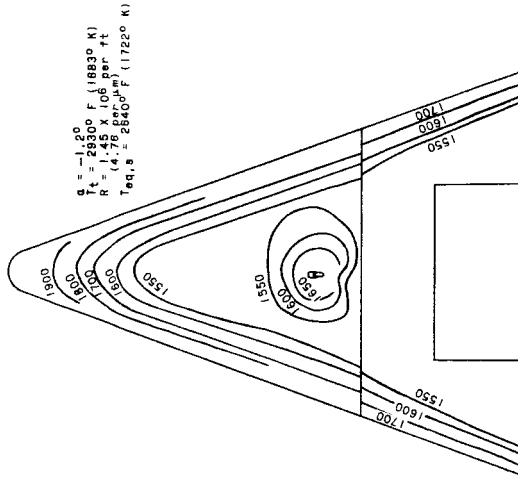
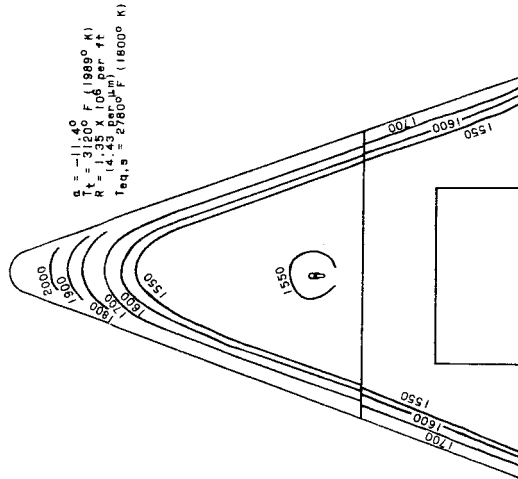
Figure 9.- Concluded.



(a) Bottom views; $R \approx 0.5 \times 10^6$ per foot (1.6 per μm).
 Figure 10.- Equilibrium isotherms on model 2B; flap extended 3° .

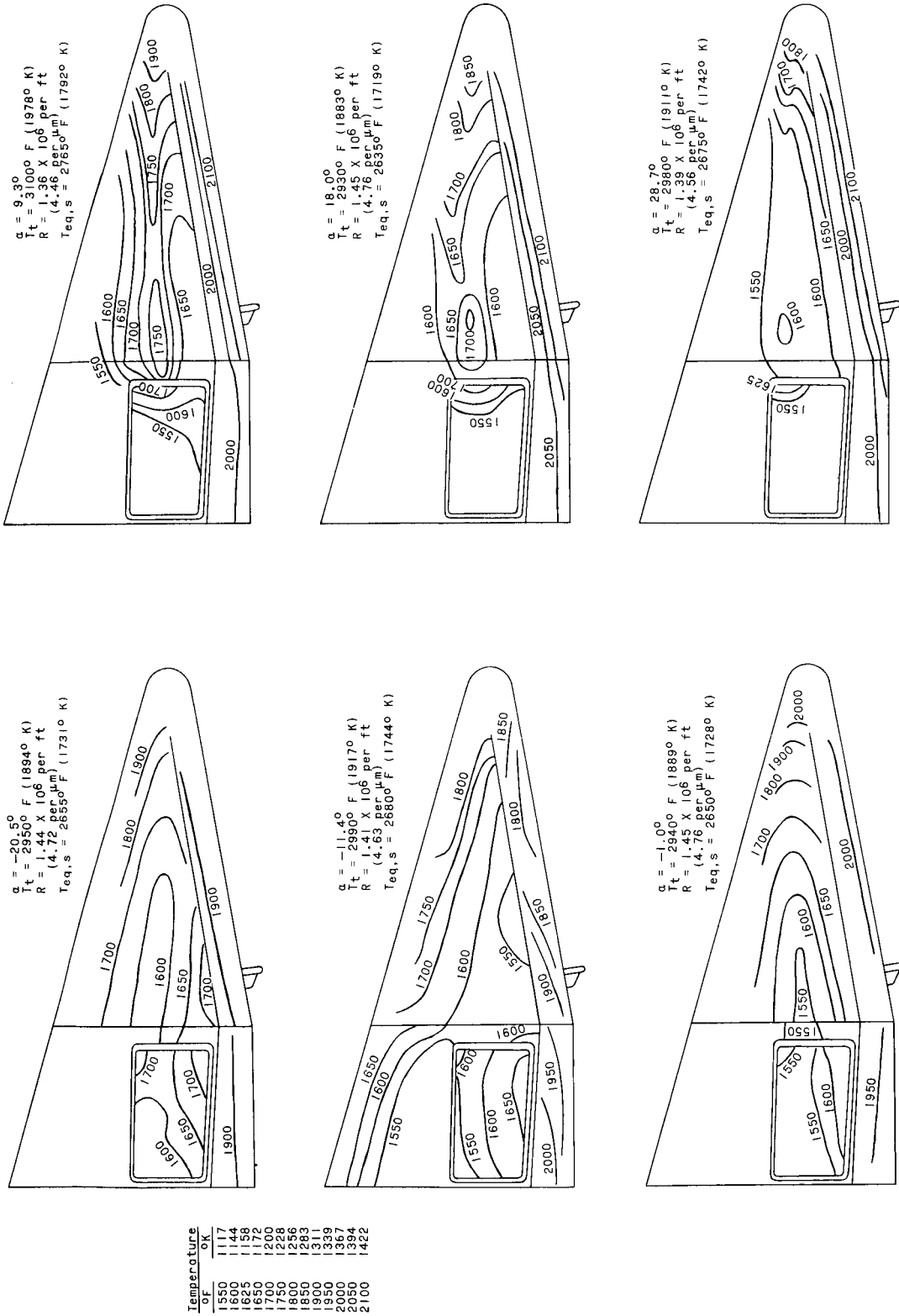


Temperature	
$^{\circ} \text{ F}$	$^{\circ} \text{ K}$
1550	1117
1600	1144
1700	1272
1750	1229
1800	1256
1900	1311
1950	1339
2000	1367
2100	1422



(b) Bottom views; $R \approx 1.5 \times 10^6$ per foot ($4.9 \text{ per } \mu\text{m}$).

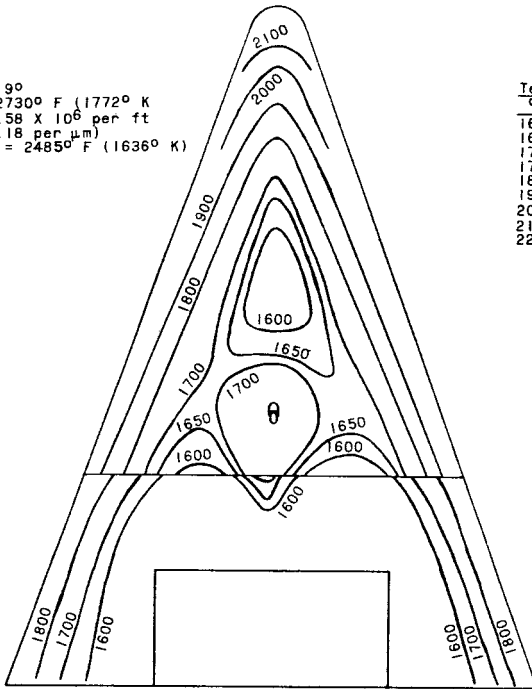
Figure 10.- Continued.



(c) Side views; $R \approx 1.5 \times 10^6$ per foot ($4.9 \text{ per } \mu\text{m}$).

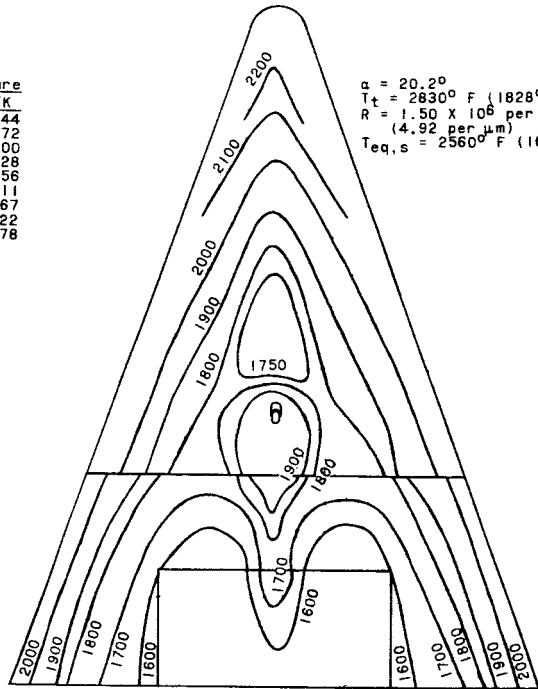
Figure 10.- Concluded.

$\alpha = 9.9^\circ$
 $T_t = 2730^\circ \text{ F } (1772^\circ \text{ K})$
 $R = 1.58 \times 10^6 \text{ per ft}$
 $(5.18 \text{ per } \mu\text{m})$
 $T_{eq,s} = 2485^\circ \text{ F } (1636^\circ \text{ K})$

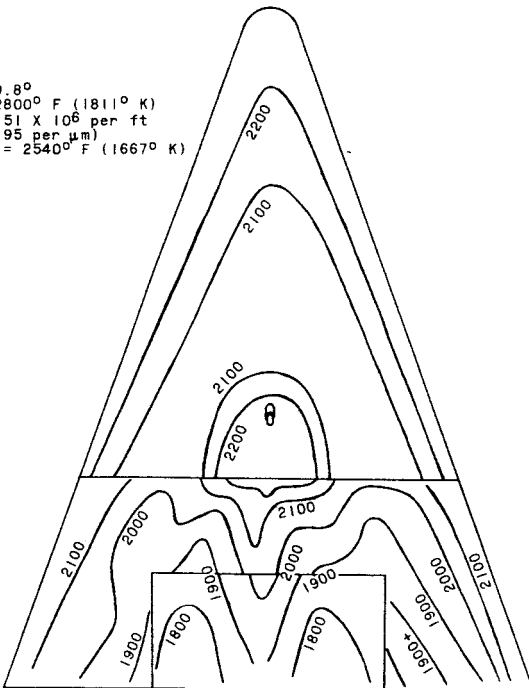


Temperature	
F	K
1600	1144
1650	1172
1700	1200
1750	1228
1800	1256
1900	1311
2000	1367
2100	1422
2200	1478

$\alpha = 20.2^\circ$
 $T_t = 2830^\circ \text{ F } (1828^\circ \text{ K})$
 $R = 1.50 \times 10^6 \text{ per ft}$
 $(4.92 \text{ per } \mu\text{m})$
 $T_{eq,s} = 2560^\circ \text{ F } (1678^\circ \text{ K})$



$\alpha = 29.8^\circ$
 $T_t = 2800^\circ \text{ F } (1811^\circ \text{ K})$
 $R = 1.51 \times 10^6 \text{ per ft}$
 $(4.95 \text{ per } \mu\text{m})$
 $T_{eq,s} = 2540^\circ \text{ F } (1667^\circ \text{ K})$



$\alpha = 20.0^\circ$
 $\text{Yaw} = 5.9^\circ$
 $T_t = 2910^\circ \text{ F } (1872^\circ \text{ K})$
 $R = 1.44 \times 10^6 \text{ per ft}$
 $(4.72 \text{ per } \mu\text{m})$
 $T_{eq,s} = 2620^\circ \text{ F } (1711^\circ \text{ K})$

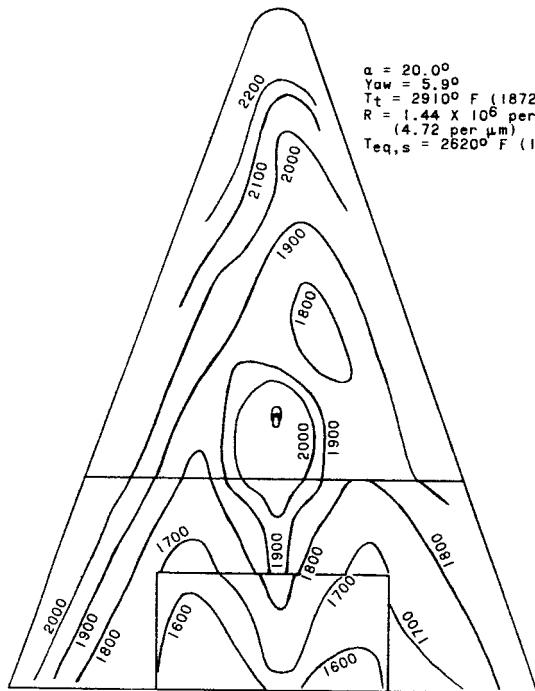


Figure 11.- Equilibrium isotherms on bottom of model 2C; flap retracted 3° .
 $R \approx 1.5 \times 10^6 \text{ per foot } (4.9 \text{ per } \mu\text{m})$.

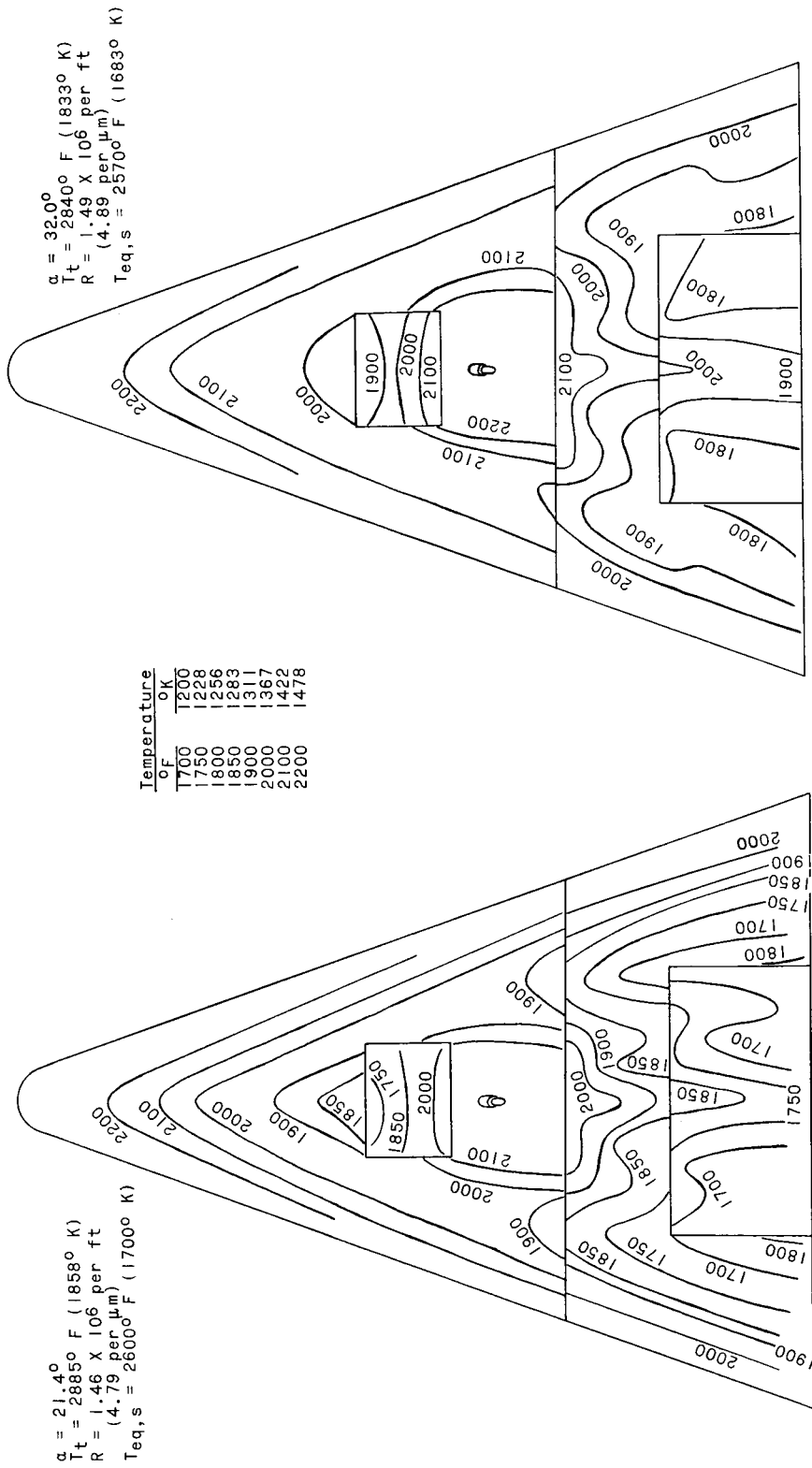
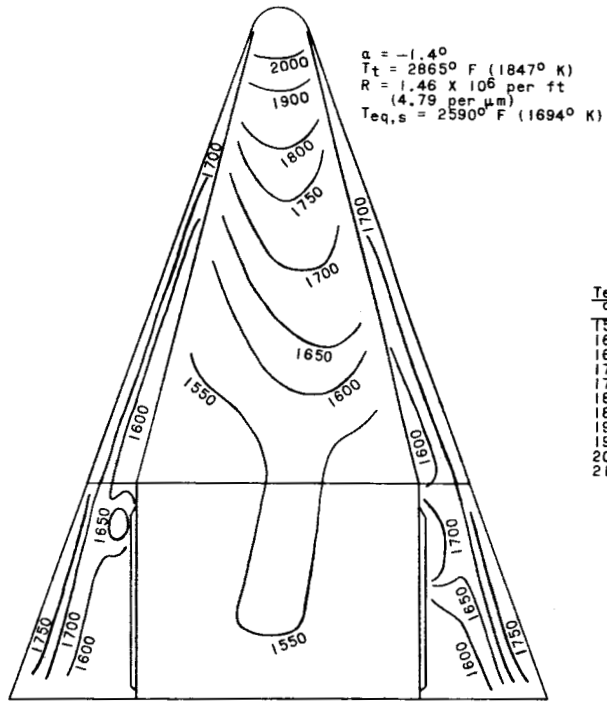


Figure 12.- Equilibrium isotherms on bottom of model 2D.
 $R \approx 1.5 \times 10^6 \text{ per foot (4.9 per } \mu\text{m)}$.



Temperature	
$^\circ \text{F}$	$^\circ \text{K}$
1550	1117
1600	1144
1650	1172
1700	1200
1750	1228
1800	1256
1850	1283
1900	1311
1950	1339
2000	1367
2100	1422

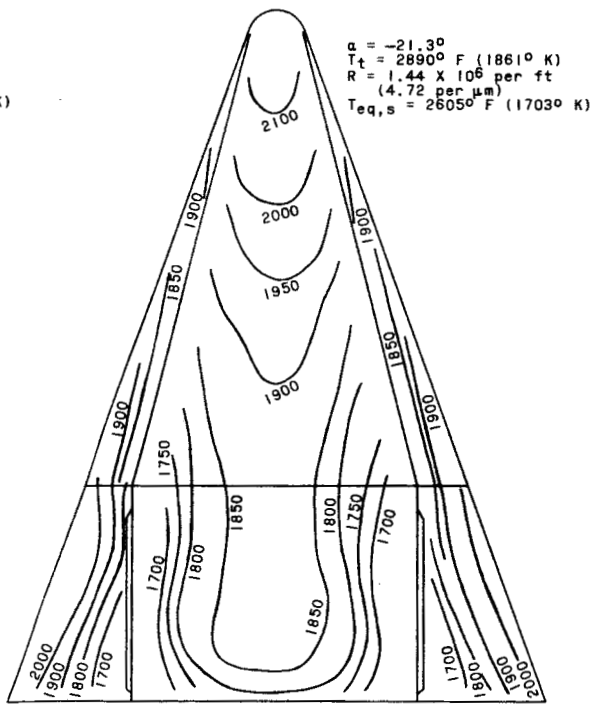
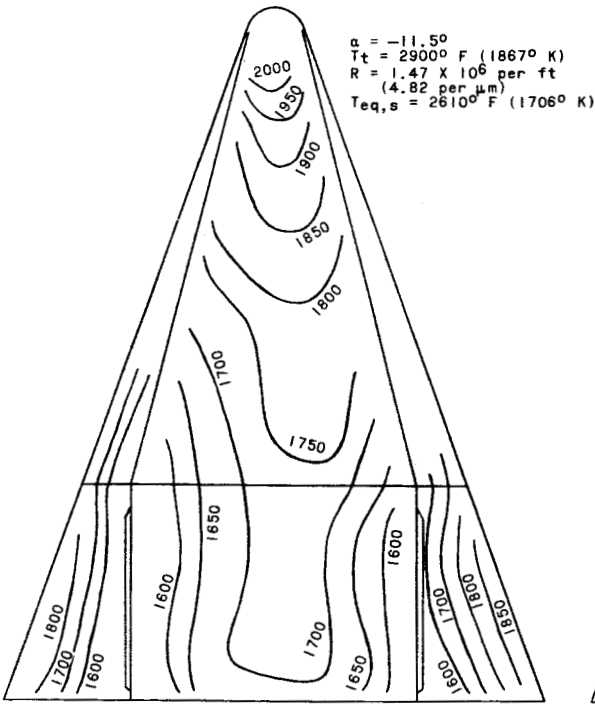


Figure 13.- Equilibrium isotherms on upper surface of model 2.
 $R \approx 1.5 \times 10^6$ per foot (4.9 per μm).

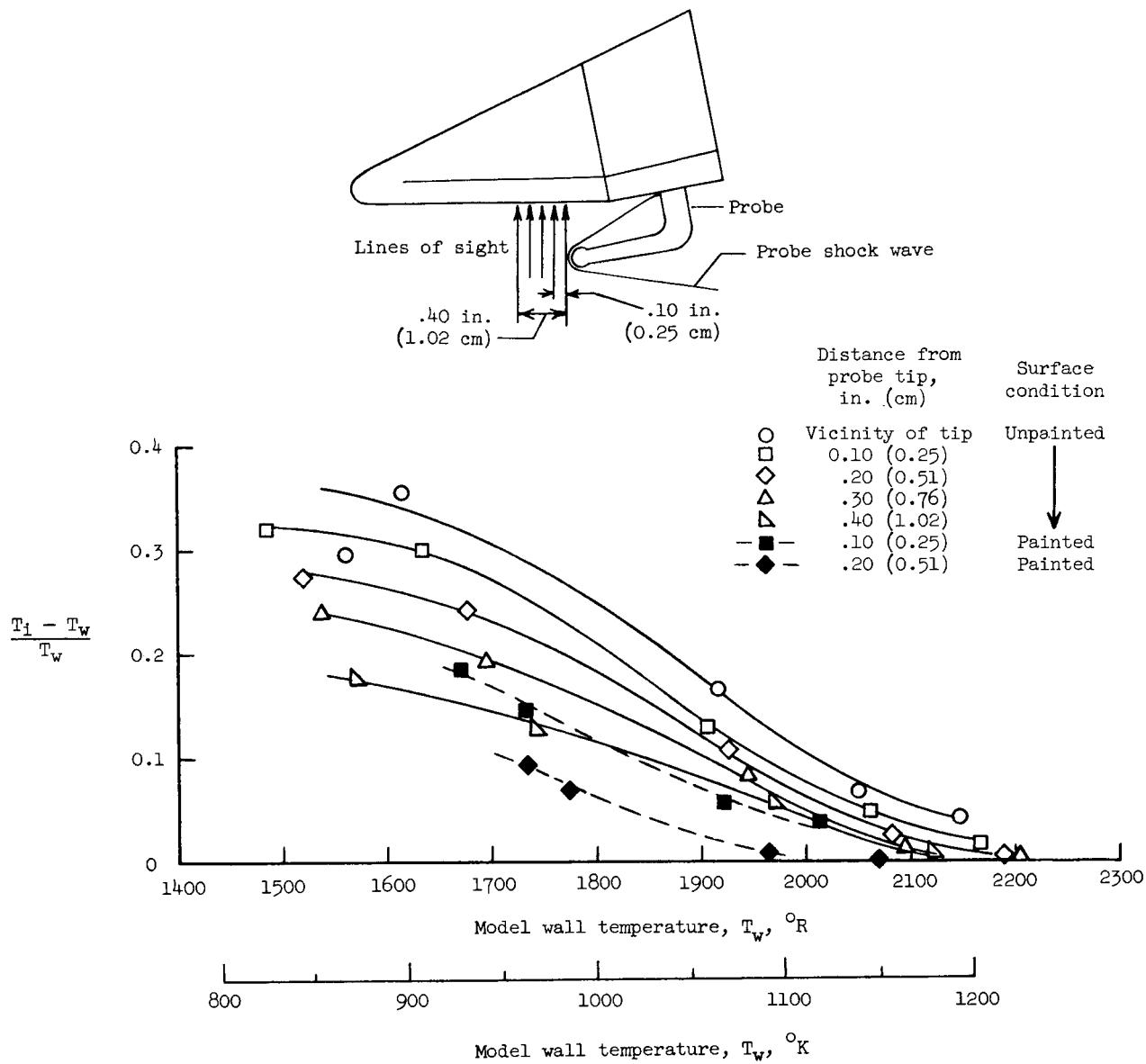
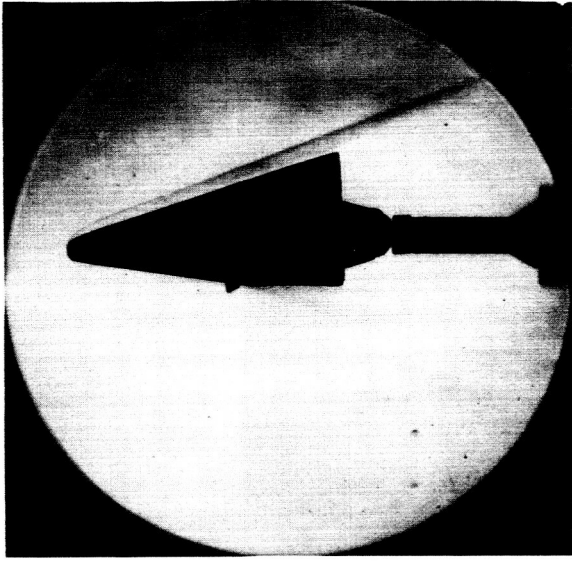
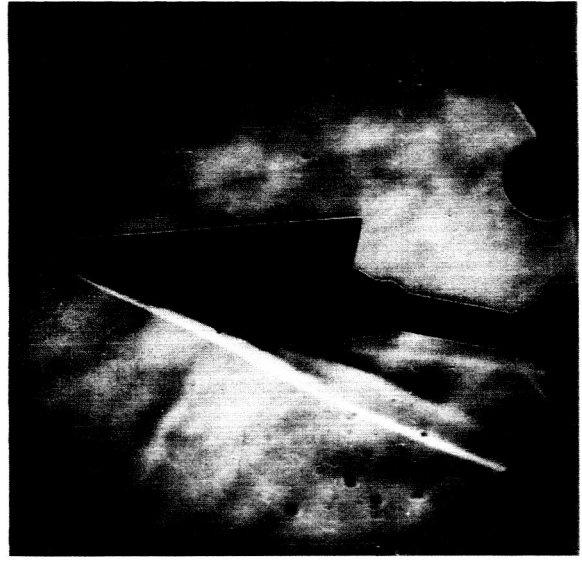


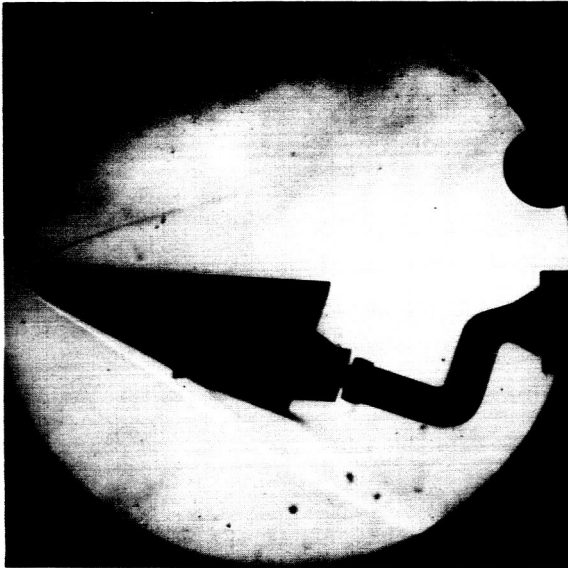
Figure 14.- Effect of reflected light on accuracy in determining surface temperatures in vicinity of high-heat source.



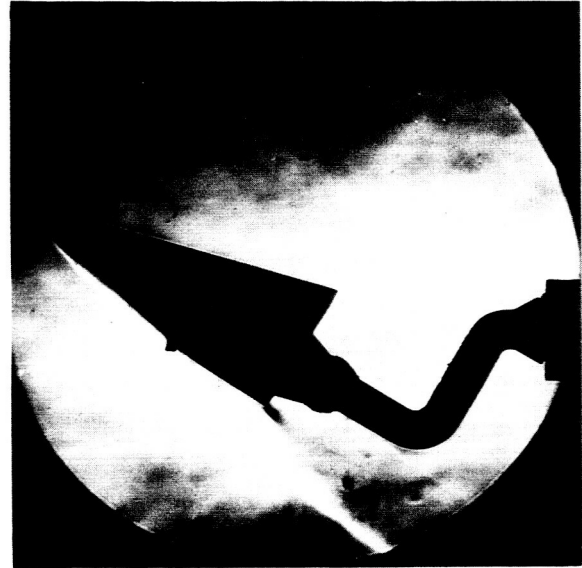
$\alpha = -1.0^\circ$



$\alpha = 11.2^\circ$



$\alpha = 20.8^\circ$

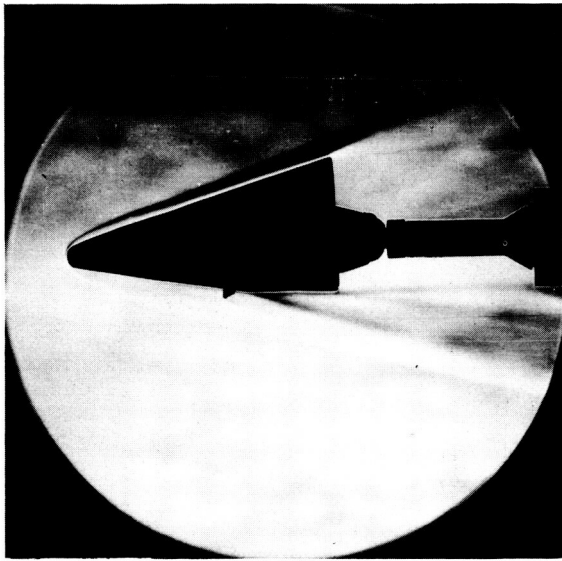


$\alpha = 31.0^\circ$

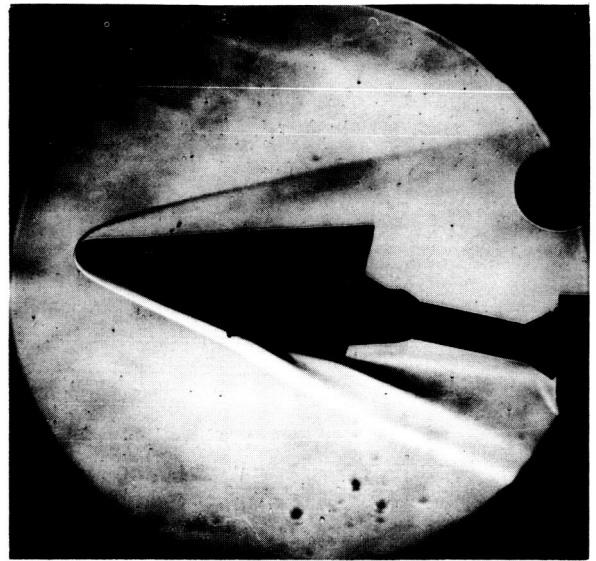
(a) $R \approx 0.5 \times 10^6$ per foot (1.6 per μm).

L-65-10

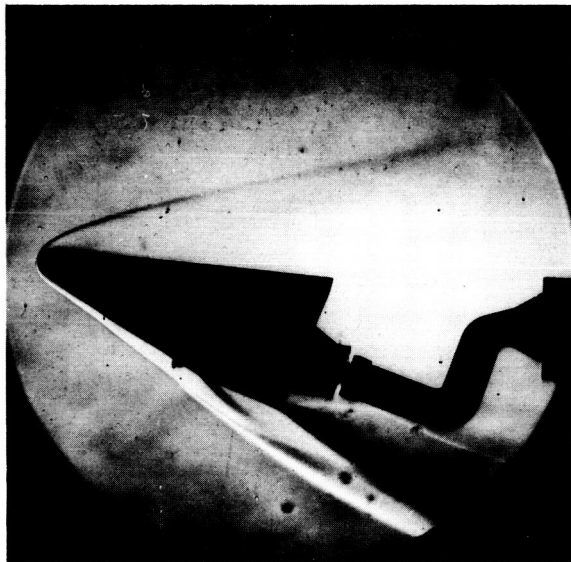
Figure 15.- Schlieren photographs of model 2.



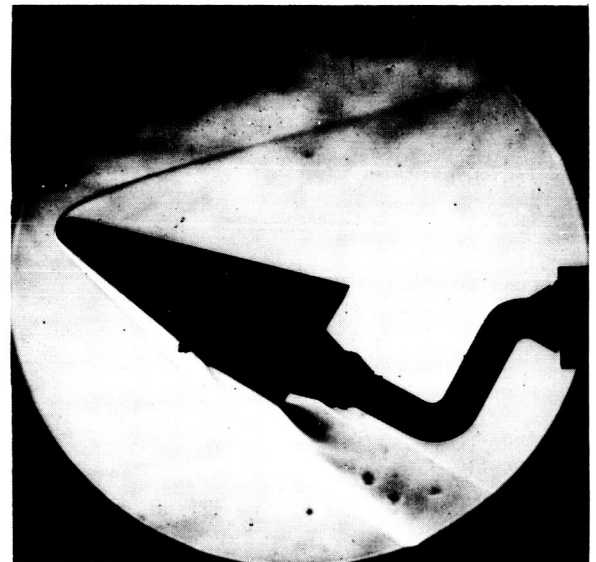
$\alpha = -1.0^\circ$



$\alpha = 11.2^\circ$



$\alpha = 20.8^\circ$



$\alpha = 31.0^\circ$

(b) $R \approx 1.5 \times 10^6$ per foot (4.9 per μm).

L-65-11

Figure 15.- Concluded.

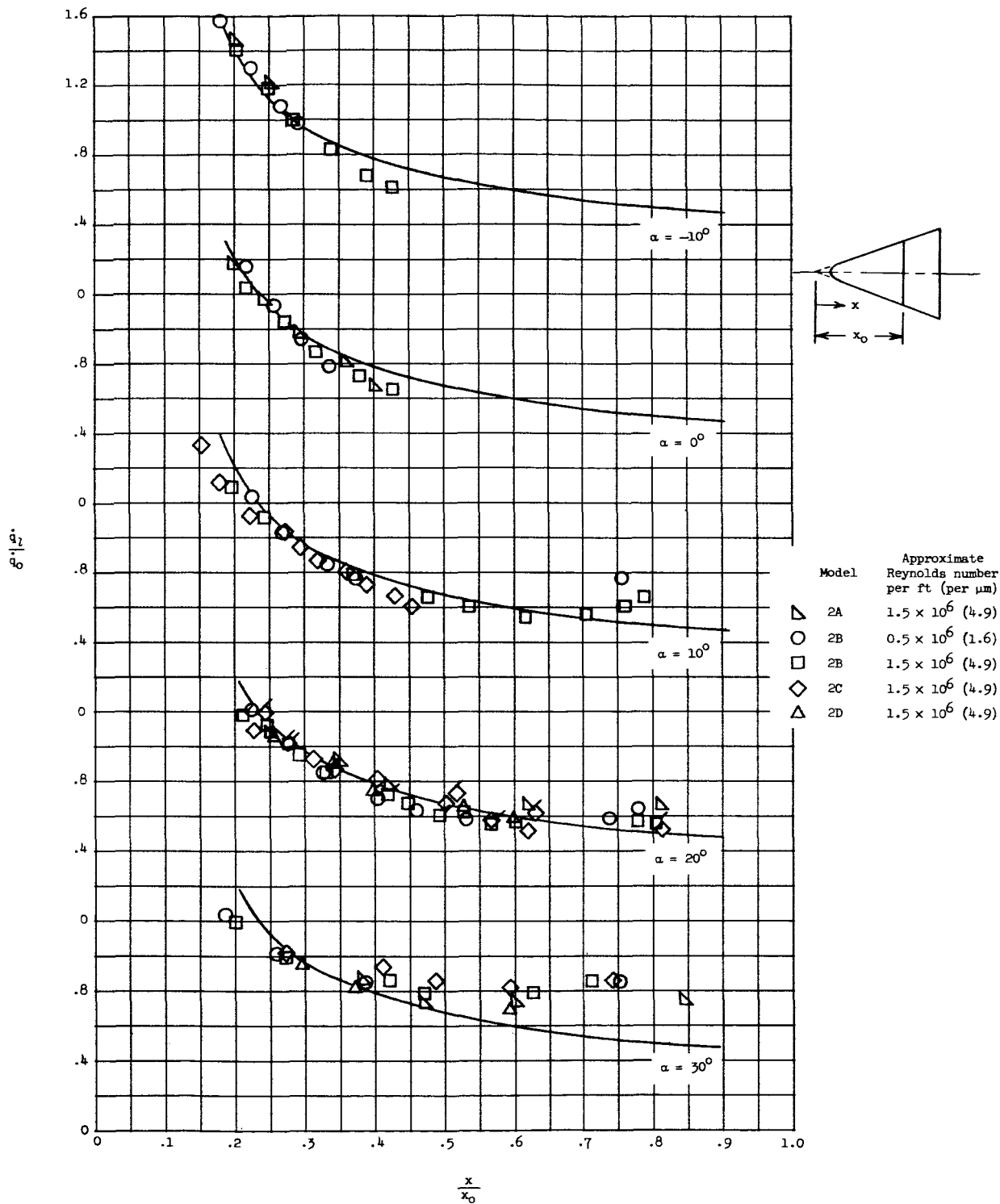
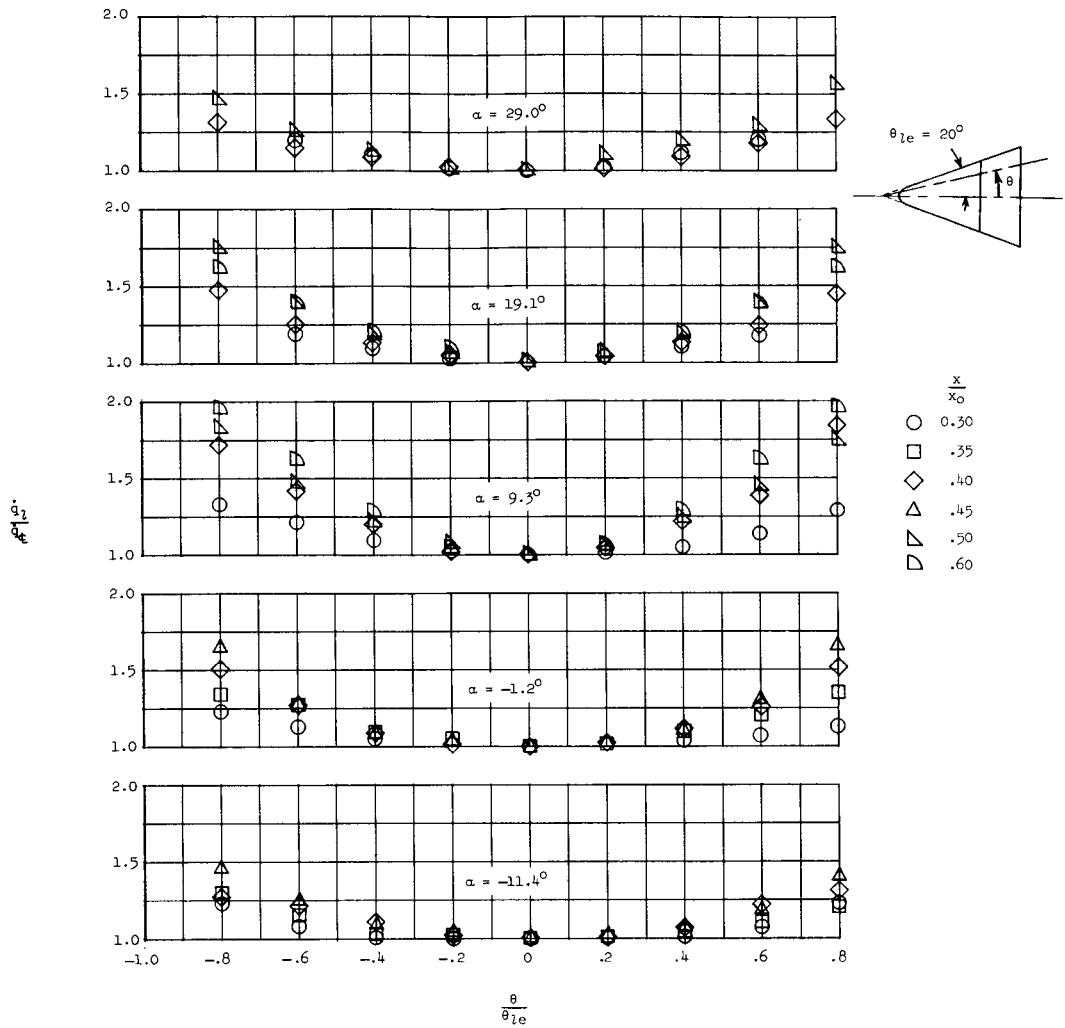
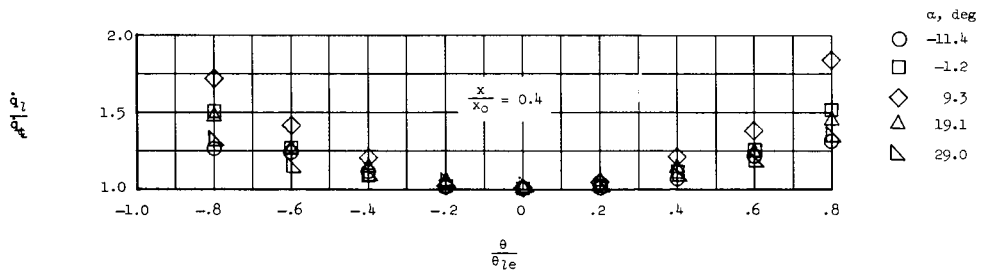


Figure 16.- Nondimensional heating rate along center line of lower surface of model 2. (Flagged symbols indicate yaw $\approx 5^\circ$; reference location is at $x/x_0 = 0.285$.)



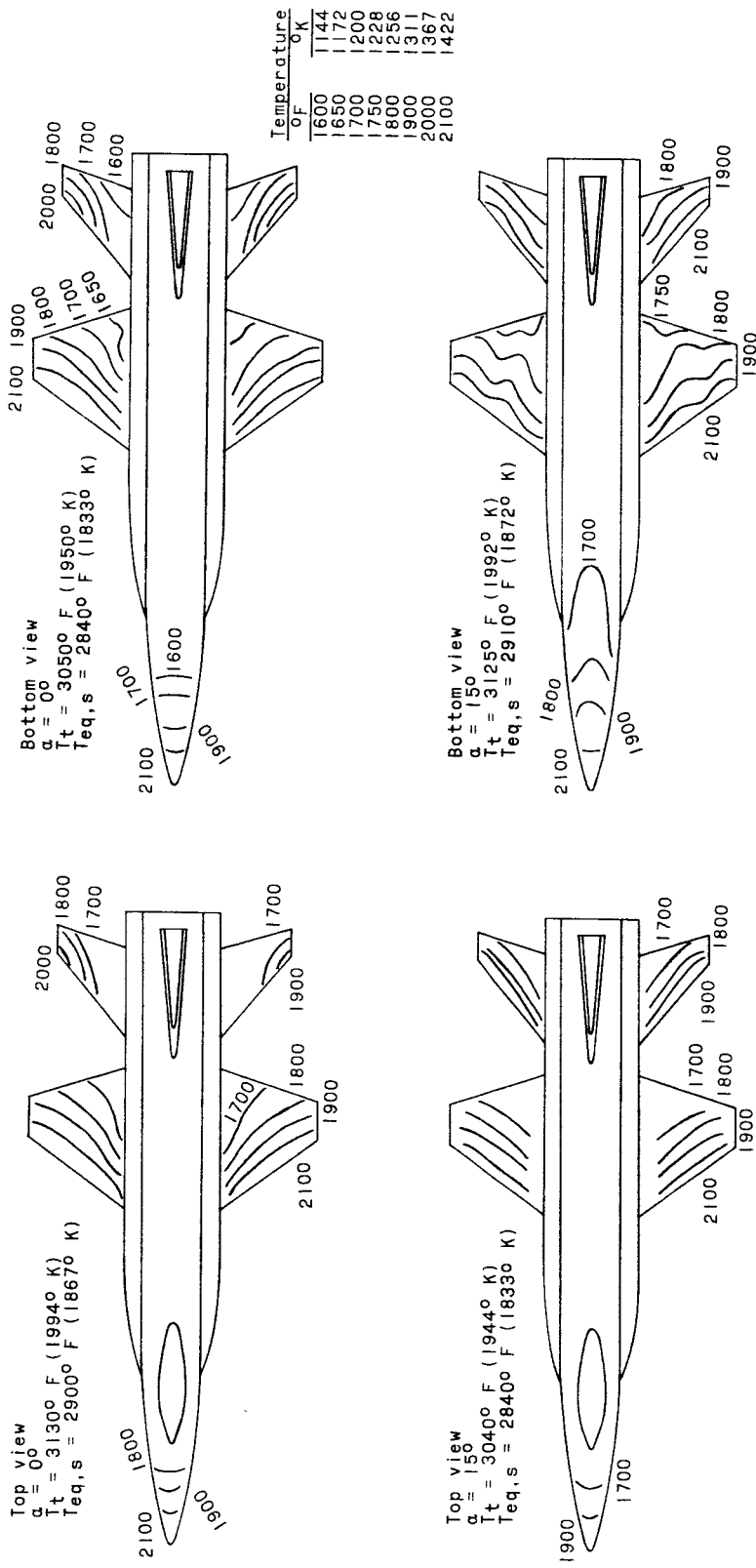
(a) Spanwise heating at several longitudinal locations for various angles of attack.



(b) Spanwise heating at several angles of attack for longitudinal station $x/x_0 = 0.4$.

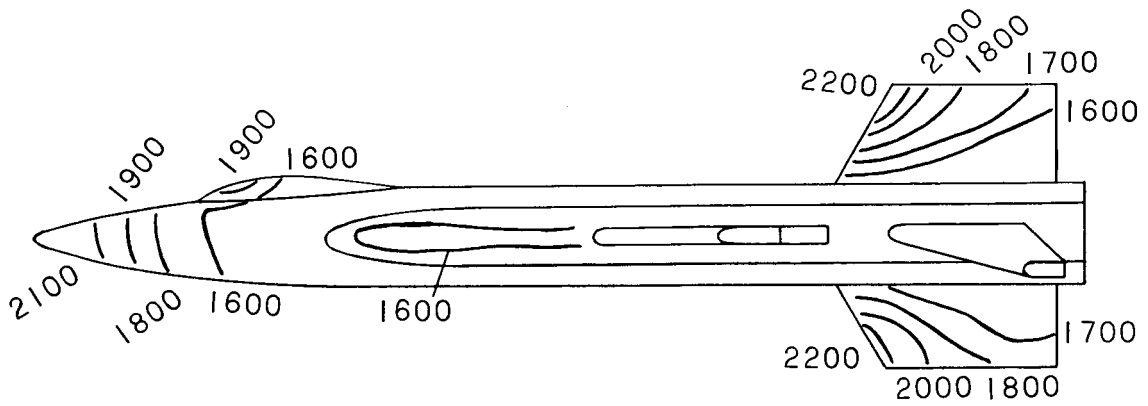
Figure 17.- Spanwise heating distribution for model 2B.

$R \approx 1.5 \times 10^6$ per foot (4.9 per μm).



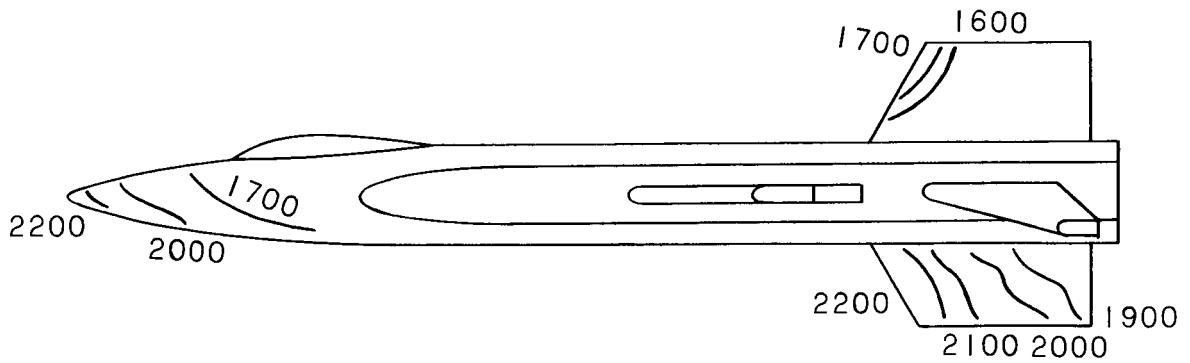
(a) Bottom and top views.

Figure 18.- Equilibrium isotherms over surface of model 3.
 $R \approx 0.75 \times 10^6$ per foot (2.5 per μm).



$\alpha = 0^\circ$
 $T_t = 3180^\circ \text{ F (2022}^\circ \text{ K)}$
 $T_{eq,s} = 2950^\circ \text{ F (1894}^\circ \text{ K)}$

Temperature	
$^\circ\text{F}$	$^\circ\text{K}$
1600	1144
1700	1200
1800	1256
1900	1311
2000	1367
2100	1422
2200	1478



$\alpha = 15^\circ$
 $T_t = 3110^\circ \text{ F (1983}^\circ \text{ K)}$
 $T_{eq,s} = 2890^\circ \text{ F (1861}^\circ \text{ K)}$

(b) Side view.

Figure 18.- Concluded.

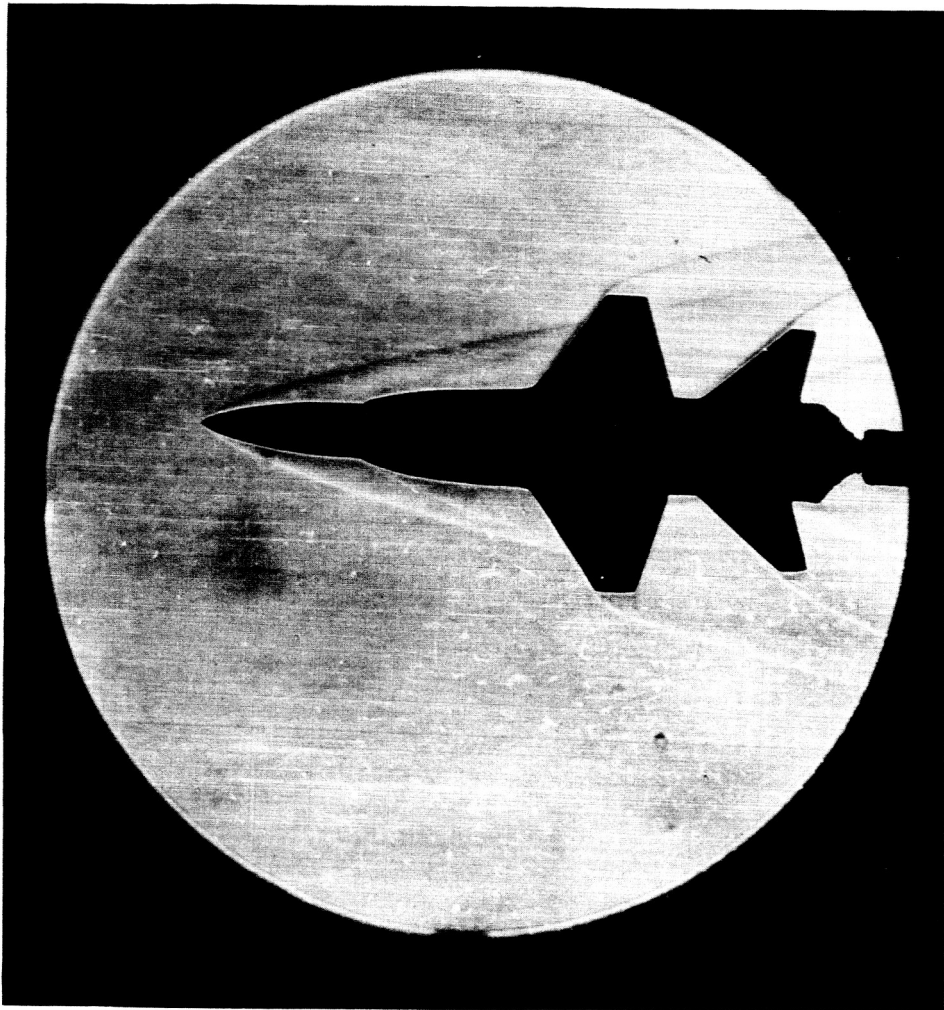


Figure 19.- Schlieren photograph of model 3. $\alpha = 15^\circ$.

L-65-12

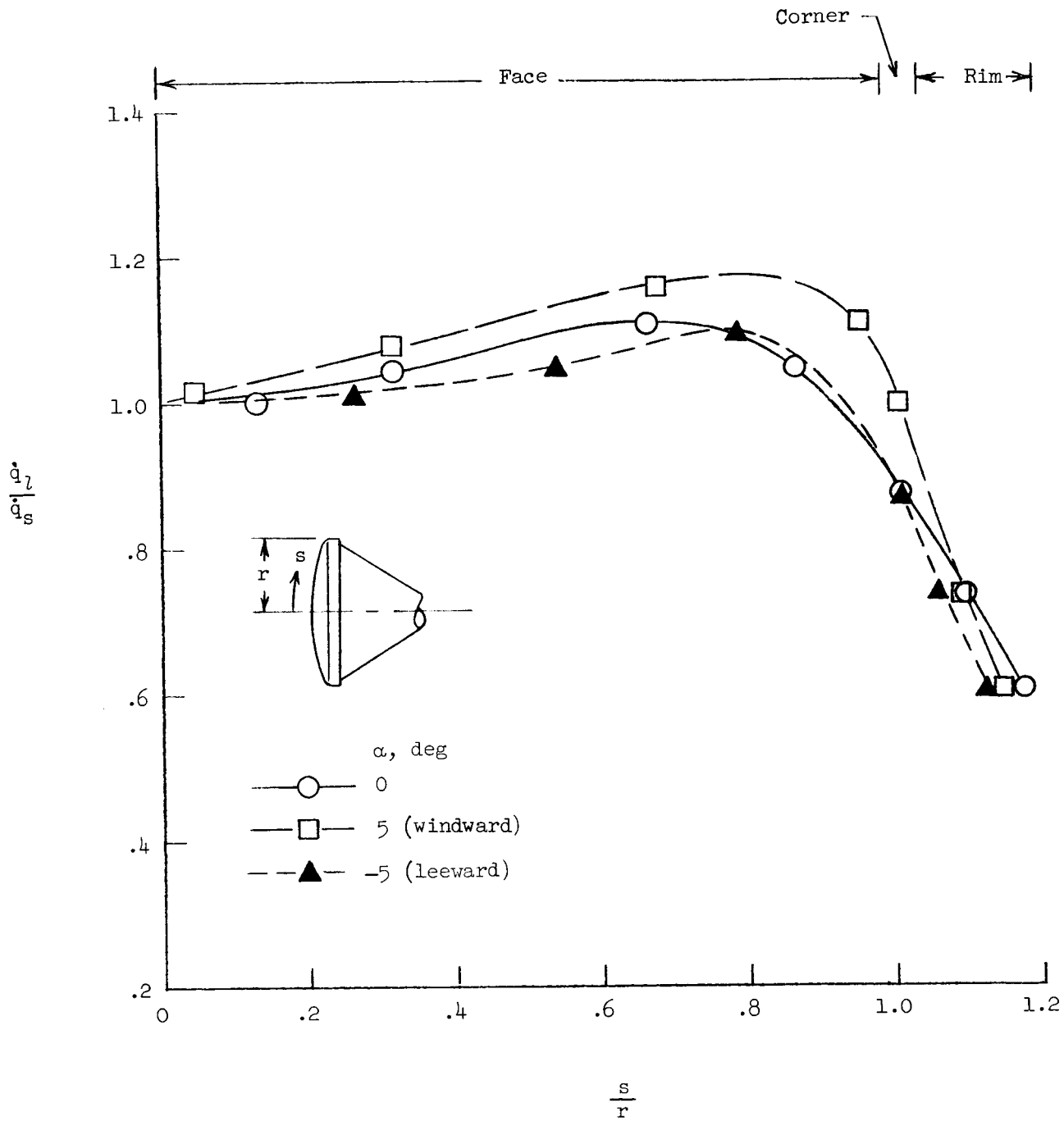


Figure 20.- Nondimensional heating around face of model 4.
 $R \approx 0.9 \times 10^6$ per foot (2.95 per μm).